Department of Physics and Astronomy

Heidelberg University

Master thesis

in Physics

submitted by

Nina Marie Elmer

born in Bünde, Germany

2022

SMEFT Russian Roulette

Is including high kinematic distributions in SMEFT global analyses worth the effort?

This Master thesis has been carried out by Nina Marie Elmer

at the

Institute for Theoretical Physics

under the supervision of

Prof. Tilman Plehn

Zusammenfassung - Hochenergetische Verteilungen in globalen SMEFT Analysen:

Mit der Entdeckung des Higgs im Jahr 2012 wurde das Standardmodell vervollständigt, aber es gibt Hinweise auf eine Physik jenseits des Standardmodells. In dieser Arbeit nutzen wir eine SMEFT, um nach Hinweisen auf neue Physik zu suchen. Abweichungen vom SM werden durch Operatoren höherer Ordnung und ihre entsprechenden Wilson-Koeffizienten in SMEFT beschrieben. Diese beitragenden Wilson-Koeffizienten können als freie Parameter behandelt werden und werden somit durch experimentelle Ergebnisse eingeschränkt. Um auch kinematisch verstärkte Wilson-Koeffizienten einzuschränken, werden zwei hohe kinematische Verteilungen verwendet. Beide Messungen stammen vom LHC, eine ist ein WH-Prozess von ATLAS und die andere ein ZH-Prozess von CMS. Sie sind ursprünglich für die Resonanzsuche konzipiert. Nachdem wir die experimentellen Ergebnisse mit Simulationen reproduziert haben, berechnen wir die SMEFT-Beiträge und addieren sie zu den SM-Vorhersagen. Diese reproduzierten Ereignisse werden dann in SFitter, einem Werkzeug für globale Analysen, implementiert. Mit SFitter sind wir in der Lage, die beteiligten Wilson-Koeffizienten einzuschränken.

Abstract - High kinematic distributions in SMEFT global analyses:

With the Higgs discovery in 2012 the Standard Model was completed, but there is evidence for physics beyond the Standard Model. In this thesis, we use the SMEFT framework to search for hints on new physics. Deviations from the SM are described through higher order operators and their corresponding Wilson coefficients in the SMEFT framework. These contributing Wilson coefficients can be treated as free parameters and are thus, constrained by experimental results. In order to constrain even kinematically enhanced Wilson coefficients two high kinematic distributions are selected.
Both measurements are from the LHC, one is a WH process from ATLAS and the other one a ZH process from CMS. They are originally designed for resonance searches. After reproducing the experimental results with simulations, we compute the SMEFT contributions and add them on top of the SM prediction. These reproduced events are then implemented into SFitter, a tool for global analyses. With SFitter we are able to constrain Wilson coefficients involved.

Contents

1 Introduction

With the proposal of the Higgs mechanism in the 1960s [1–3] and its experimental confirmation in 2012 at the Large Hadron Collider (LHC) [4–6], the last missing piece of the Standard Model (SM) was discovered. This was the last breakthrough in particle physics. Yet, the SM does not answer all remaining and open questions in particle physics regarding the SM. One of these questions addresses the Higgs boson and its light mass compared to the much heavier top quark [7]. Other questions left open by the SM are the nature of Dark Matter [8], the neutrino masses [9] or the matter-anti-matter asymmetry in the universe [10]. While many new models have been developed to answer some of these questions, none of them have been experimentally confirmed, nor has the LHC found any significant deviations from the SM.
In this thesis, an agnostic framework is selected, by considering an effective field theory (EFT) as an extension of the SM. This approach for new physics is called the SM effective field theory, or for short SMEFT [11]. Since the SMEFT goes beyond the four dimensions of the SM, higher order operators are entering and with them new Wilson coefficients. These new coefficients can be treated as free parameters. Experimental results can be used to constrain these Wilson coefficients from the SMEFT. Some of the Wilson coefficients are kinematically enhanced and, thus, mostly visible in high energy regions. To be able to constraint these, high kinematic distributions provided by the ATLAS and CMS collaborations can be used.

In order to constrain kinematically enhanced coefficients, we investigate two measurements of high kinematic distributions and implement them into SFitter, a global analysis tool. One of these measurements is a WH search provided by the ATLAS collaboration in Ref. [40] and the other one is a ZH search provided by the CMS Collaboration in Ref. [25]. This is done to update older measurements and add more high kinematic distributions to other distributions with lower kinematics. An overview about already implemented distributions can be found in Ref. [41]. There exists an older ATLAS WH implementation from Ref. [42] already in SFitter, coming from early LHC Run II results. In this thesis, we investigate if this newer measurement has greater constraining power than the previously implemented measurement. To check this potential improvement and replace the old measurement is one goal of this thesis. In contrast, the ZH process is the first high kinematic distribution from the CMS collaboration added to SFitter. With this one, the global fit is extended by one more measurement, coming from a different group and, thus, hopefully provides us with new insights on the constraining power of the coefficients

and their correlations. In the end, the results from the newly implemented measurements will be compared to previous results in up to eight dimensional global fits.

The thesis is structured in the following way: Chapter 2 provides an overview of the SM Higgs sector, together with typical production and decay channels of the Higgs boson. Furthermore, it gives some insight on the EFT-framework. The next chapter 3 explains the HVT signal, used in the ZH implementation. The following chapter 4 describes the tools used in this thesis. First, the MADGRAPH [26, 27]-PYTHIA [28]-DELPHES [29] chain, used for event generation and reproduction of the experimental data sets, is covered. After the event generation, SFitter [30], the global analysis framework, is explained. With the tools described, we can move on to the actual implementation of the VH processes in chapter 5. In chapter 5.1 the implementation of the WH process is discussed and in chapter 5.2 the implementation of the ZH measurement. Lastly, chapter 6 shows a global analysis using the two newly implemented measurements. Also, the new results are compared to already existing implementations of high kinematic distributions in SFitter. A brief summary of the results are given in chapter 7.

2 SMEFT in the Higgs sector

This chapter covers the theoretical background of the thesis and is loosely based on Ref. [12–14]. We will start with a short summary of the Higgs sector in the SM and then continue with leading order production and decay channels of the Higgs boson. The second part of the chapter gives a brief introduction into the framework of effective field theories and their use as extensions of already existing theories, like the SM.

2.1 Standard Model and Higgs physics

The particle content of the SM includes four gauge bosons, one scalar particle, also known as the Higgs boson, and 12 fermions, divided into six quarks and six leptons. Another key aspect is the fundamental symmetries of the SM, because both particle content and symmetries have to be included in order to build up a proper effective field theory from the SM.
The structure of the SM consists of a $SU(3)_C \times SU(2)_L \times U(1)_Y$ gauge group and its corresponding symmetries. These fundamental symmetries include gauge symmetries and space-time symmetries, for example Lorentz or CPT symmetry.

Since the focus is on the Higgs sector, which is part of the electroweak symmetry, $SU(2)_L \times U(1)_Y$, one can neglect contributions from $SU(3)_C$. This $SU(3)_C$ group is responsible for describing QCD effects and the strong force in the SM.
The electroweak symmetry breaking (EWSB) in the electroweak sector, provides a mechanism to generate the masses of the $W^{\pm}$ and Z boson. In the SM, the EWSB is realized with a complex scalar doublet ϕ called the Higgs field [1–3].
The Lagrangian of the SM Higgs sector can be described in the following way

$$\begin{aligned} &\mathcal{L}_{\text{Higgs}} = (D_\mu \phi)^\dagger (D^\mu \phi) - V(\phi) + \mathcal{L}_{\text{Yukawa}}, \\ &\text{with } V(\phi) = \mu^2 \phi^\dagger \phi + \lambda (\phi^\dagger \phi)^2 \\ &\text{and } \mathcal{L}_{\text{Yukawa}} = - \sum_{\text{generations}} \left(y_u \begin{pmatrix} \bar{u} \\ \bar{d} \end{pmatrix}_L \tilde{\phi}\, u_R + y_d \begin{pmatrix} \bar{u} \\ \bar{d} \end{pmatrix}_L \phi\, d_R + y_l \begin{pmatrix} \bar{\nu} \\ \bar{l}^- \end{pmatrix}_L \phi\, l_R \right). \end{aligned} \tag{2.1}$$

$V(\phi)$ defines the Higgs potential, with its real parameters μ^2 and λ. In the Yukawa-Lagrangian the y_i's denote the Yukawa couplings as complex matrices in flavor space, and the subscript L indicates the left-handed version of the fermions, where u denotes up quarks, d down quarks and l leptons for each of the three generations. $\tilde{\phi}$ is defined as $\tilde{\phi} = i\sigma_2 \phi^\star$ in the Yukawa Lagrangian.

The covariant derivative appearing in $\mathcal{L}_{\text{Higgs}}$ is defined as

$$D_\mu \phi = \left(\partial_\mu + ig \frac{\sigma^a}{2} W_\mu^a + i \frac{g'}{2} B_\mu \right) \phi, \tag{2.2}$$

where the B_μ denotes the gauge boson from the $U(1)_Y$ gauge group, W_μ^a the one from the $SU(2)_L$ gauge group and g' and g are the corresponding coupling constants, with σ the Pauli matrices.
In the case $\mu^2 < 0$, the minimum energy state is not at $\phi = 0$, but at

$$|\langle \phi \rangle|^2 = \frac{v^2}{2} = \frac{-\mu^2}{2\lambda}, \tag{2.3}$$

in this equation v is the vacuum expectation value (vev) of ϕ. With this minimum condition only the absolute value of the minimum is determined and not its direction.
By choosing a direction, the SM gauge symmetry is spontaneously broken into $U(1)_Q$, the electromagnetic sector. This resulting scalar doublet can be written in the following way

$$\phi = \frac{1}{\sqrt{2}} \begin{pmatrix} -w_2 - iw_1 \\ v + H + iw_3 \end{pmatrix} \tag{2.4}$$

with v the vev of the physical Higgs field H and w_i the Goldstone bosons which stem from the spontaneous symmetry breaking. The Goldstone bosons w_i combined with the gauge bosons W^a and B from Eq. (2.2) result in the mass eigenstates γ, Z and $W^\pm$. Lastly, the remaining degree of freedom is the scalar field H, the physical Higgs boson.
Writing the Higgs doublet of the Lagrangian in Eq. (2.1) in unitary gauge and ignoring the Goldstone bosons, leaves us with

$$\phi = \frac{1}{\sqrt{2}} \begin{pmatrix} 0 \\ v + H \end{pmatrix}. \tag{2.5}$$

Inserting Eq. (2.5) into the Lagrangian in Eq. (2.1) gives an expression for the Higgs mass $m_H = -2\mu^2 = 2\lambda v^2$, with $m_H = 125$ GeV [4, 5].

Since H and v always show up in a combination, the same terms inducing couplings of fermions and bosons to the Higgs boson, are also responsible for the mass of these particles. With this in mind, there is a proportionality between the H boson coupling to other SM particles, denoted as x. These particles obtain their mass from the EWSB relation, namely $g_{hx} \sim m_x$.

Production and decay of the Higgs

Since the coupling of the Higgs boson to the SM particles is proportional to their masses, the Higgs boson predominately couples to the heavy particles. So the main

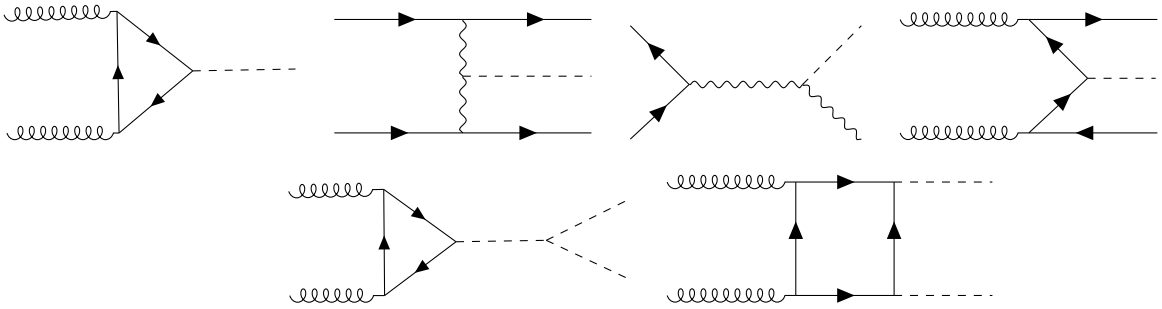

Figure 2.1: Higgs production processes and their corresponding Feynman diagrams. Upper Row: left: gluon fusion (ggF), left center: vector boson fusion (VBF), right center: associate production involving a vector boson, right: $t\bar{t}H$ production. Lower Row: two di-Higgs production diagrams.

production processes involves the W, Z boson and t quark.

At the LHC the Higgs boson is mostly produced via gluon-gluon fusion (ggF) with a large contribution from the t quark in a loop and a minor one from the b quark. The corresponding Feynman diagram to this process is the upper left in Fig. (2.1). Another process is vector boson fusion (VBF), which is a quark-initiated process shown in the second from left process in Fig. (2.1). In the end there are two highly energetic jets produced together with the Higgs, pointing back-to-back in the two forward directions of the detector. This leads to a large invariant mass m_{jj}. Another important aspect is, that there is little to no color exchange between the two initial quarks leading to nearly no QCD radiation [15]. With these two quantities of VBF, one can reduce the QCD background, consisting mostly of single central jets, by requiring two leading jets with a large invariant mass m_{jj}.
W and Z bosons not only play a role in VBF but also in the associated Higgs production with a vector boson, shown in the second from right Feynman diagram of Fig. (2.1). This process is also referred to as Higgs-strahlung. The final state gauge boson helps to distinguish the Higgs from the QCD background.
Lastly, another possible production process is the associated production with a $t\bar{t}$ pair, shown in the right process in Fig. (2.1), but not discussed further in this thesis. The corresponding production cross-sections are listed in Tab. (2.1), in a pp collider with $\sqrt{s} = 13$ TeV.

The cubic Higgs self-coupling, denoted as λ in the potential, enables us to obtain an insight into the structure of the Higgs potential in Eq. (2.1), by measuring the di-Higgs production. The two most relevant Feynman diagrams for this process are shown in the lower row of Fig. (2.1). The large Higgs mass makes the di-Higgs production phase-space suppressed and additionally, there is a negative interference between the two dominant diagrams entering the process. In fact the cross-section

for di-Higgs production is a factor 16 smaller than the cross-section from Higgs production with a top-pair involved, see Tab. (2.1). But this negative interference between the two diagrams make the di-Higgs production sensitive to new physics with modified Higgs sectors. Such models might reduce the cancellations or enhance its cross-section, so that it is easier to detect.

With the Higgs coupling to all massive particles in the SM, it has a broad decay spectrum. The favoured one is the decay into a $b\bar{b}$ pair, the heaviest allowed particle combination. But it is not the most sensitive to experimental signatures in the large QCD background.
A decay mode, that is easier to detect, is the decay into τ leptons with corresponding neutrinos, presenting as missing energy in the detector. Even a decay into WW and ZZ pairs where the gauge bosons decay into four leptons are easier to detect. Due to the large mass of the two vector bosons, one has to decay off-shell, because m_H is below the threshold for a WW or a ZZ production. So the decay process $H \to ZZ \to 4l$ has an extremely clear signal but a small branching ratio, as listed in Tab. (2.2).
Another possible decay mode is a loop-induced decay into a $\gamma\gamma$ pair, with a dominant contribution from a W loop, which can interfere destructively with a top-loop. In this case the clear signal from the photon pair on top of a QCD background make it easier to detect, despite its small branching ratio of 0.23%.
With this in mind and the large QCD background, there are two crucial channels to detect the Higgs-boson, also referred to as the golden channels. These are the decay process into a ZZ pair followed by a decay into $4l$ and the di-photon decay channel, in which the Higgs was discovered [4, 17].

Every detail presented above is included in standard Higgs physics. With the SMEFT, we are interested in deviations from the SM Higgs physics. This means we need to include both standard and non-standard Higgs measurements to get a better handle on all the Wilson coefficients involved. In this thesis, we will discuss one non-standard measurement in particular: VH production with H decaying

production channel	cross section [pb]
ggF	48.58
VBF	3.782
WH	1.373
ZH	0.8839
$t\bar{t}H$	0.5071
Di-Higgs	0.03105

Table 2.1: Higgs boson production channels and their corresponding cross-section predictions for the LHC Run II in a pp collision with $\sqrt{s} = 13$ TeV [16].

decay channel	Branching ratio
$b\bar{b}$	0.582
$WW^\star$	0.214
gg	0.082
$\tau\tau$	0.062
$c\bar{c}$	0.029
$ZZ^\star$	0.026
$Z\gamma$	0.002
$\gamma\gamma$	0.002

Table 2.2: Predictions for the branching rations of the Higgs boson in the Standard Model, taken from [16].

into a $b\bar{b}$ pair and V decaying into leptons in the high invariant mass region. It is interesting because is can lead to better constraints on kinematically enhanced Wilson coefficients.

2.2 Effective Field Theory for the Standard Model

The previously introduced SM describes many findings from the LHC and other colliders correctly and accurately but there are still some unsolved problems and open questions the SM cannot explain. For example, there is no good explanation for massive neutrinos in the SM or Dark Matter in the universe. Other problems on a smaller scale are fine-tuning problems, like the relatively small Higgs mass compared to the large Planck scale. Unfortunately, there are even more unanswered questions in the SM, so one can say that it is an incomplete theory and needs some corrections or extensions.

The LHC has not discovered signs of new physics yet. This suggests that new physics is probably taking place at higher energies that we are currently unable to reach with the LHC or any other current collider. With this in mind, we have to look for indirect signs of new physics, since we might not be able to find direct hints or signs. Such indirect signs could be deviations from the SM in the high-energy tail region of experiments. For example, a rise in the tail region could be linked to the beginning of a resonance, while the position of the actual peak is currently not reachable by the LHC.
There are many different models to describe the effects of new physics, but it would be inefficient and time consuming to study them all and find the best-fitting model. So there is a need for an adaptable, model-independent way to describe the phenomena of new physics [18].

This is where effective field theories (EFTs) become useful. They combine theory with data analysis, by reducing a full theory to an EFT, whose coefficients can be constrained by experimental data.
EFTs are a well-established and fundamental theoretical concepts in physics with an underlying concept of scale separation. This means that the behaviour of a system at a given scale is independent of the details at a completely different scale, either much larger or smaller than the initial scale. For example we do not consider the movement of the quarks in an atom at a car crash.
So while physics happening at high energy scales can be described by an underlying theory, we do not need to know every detail about the underlying theory in order to describe physics occurring at lower energy scales. In order to construct an EFT, there is no need to know the complete theory. With this in mind, EFTs are conceptually simpler and it is often easier to compute quantities of physical interest in an EFT rather than the full theory. The approximation of the EFT is only valid as long as the energy of the relevant process E is smaller than the mass scale of new physics Λ:

$$E \ll \Lambda. \tag{2.6}$$

The Fermi theory for weak interactions is a good example for an EFT with the SM as the underlying full theory [19]. In the limit of small momentum p compared to the W mass m_W, the three-point vertex becomes a four-point vertex and, as a heavy particle, the W boson can be integrated out, and the propagator expressed as a Taylor-expansion in p^2/m_W^2:

$$\frac{1}{p^2 - m_W^2} = -\frac{1}{m_W^2} + \frac{p^2}{m_W^4} \approx -\frac{1}{m_W^2}, \qquad p^2 \ll m_W^2. \tag{2.7}$$

This change in the propagator is shown in the Feynman-diagram for the β decay in Fig. (2.2), where the original diagram with two three-point vertices from the SM is reduced to a four-point vertex diagram. In this case, the cut-off scale is around $\Lambda \approx m_W$ with the SM as the fundamental theory behind. So in the low-energy limit of an EFT, as seen in the Fermi's theory, the heavy fields decouple and thus cannot be produced on-shell, while they are also heavily suppressed off-shell. Some more examples and detailed explanations can also be found in Ref. [20].

Possible deviations from the SM, can be modelled by the SM effective field theory (SMEFT) which is the EFT with the SM as the underlying theory [21]. The SMEFT is constructed with a bottom-up approach, starting with an existing theory and not knowing the full theory behind it. Falling back to mass-dimension 4, the SMEFT should end up with the SM, so there are only two constraints to build the SMEFT. First, it should have the same particle content as the SM, because new particles at higher masses are integrated out and, thus, contributions from these particles can be

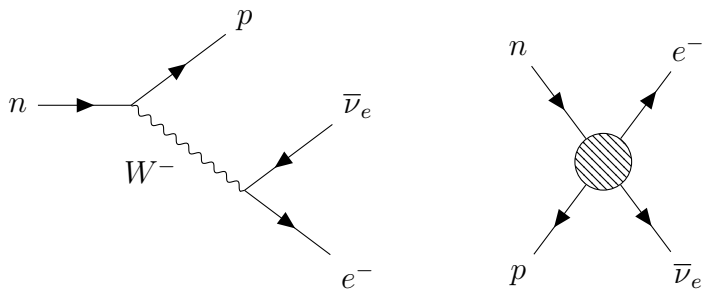

Figure 2.2: β decay as an example of an effective field theory with the SM as full theory behind it.

seen at higher order interactions with the SM particle content. Second, it should retain the fundamental symmetries of the SM, like the gauge, CPT or Lorentz symmetry. If the fundamental symmetries are removed, the EFT is changed and will no longer represent the SM. However, accidental symmetries, such as lepton number conservation, do not have to be retained.
In order to be able to fall back to the SM at dim. 4, the higher order dimensions are suppressed by a factor Λ^{-1}, thus giving a general form of the SMEFT

$$\mathcal{L}_{\text{SMEFT}} = \mathcal{L}_{\text{SM}} + \sum_{i,d} \frac{c_i^{(d)}}{\Lambda^{d-4}} \mathcal{O}_i^{(d)}, \tag{2.8}$$

with c_i the Wilson coefficients [22]. These can be interpreted as coupling constants of the EFT and thus are fixed by masses and couplings in the full theory. If the full theory is unknown, they are treated as free parameters. The $\mathcal{O}_i^{(d)}$ in the SMEFT are the corresponding operators of mass-dimension d and should satisfy the same fundamental symmetries as in the SM. At dim. 5, only one new operator is added, the so-called Weinberg operator, responsible for neutrino masses. A part of the dim. 6 operators are responsible for SMEFT contributions to Higgs physics, so the main focus will be on these operators. Dim. 8 and higher dimensional operators are assumed to be much more suppressed and thus not considered in this thesis.

With the full SMEFT framework, we can describe any UV complete theory which falls back to the SM in the low-energy limit. The SMEFT is just an approximation and, thus, the full theory behind it is unknown. With this in mind, the Wilson coefficients can be treated as free parameters and constrained by experimental data. One thing to keep in mind when constraining the Wilson coefficients, is that it is only possible to extract values for $c_i/\Lambda^{(d-4)}$ from these analyses. So the results can be interpreted for a specific Λ or they can give constraints on the term $c_i/\Lambda^{(d-4)}$, if no specific value of Λ is chosen.

Since mostly dim. 6 operators play a role in the contributions to Higgs physics for the considered high kinematic distribution at leading order, the focus is on these

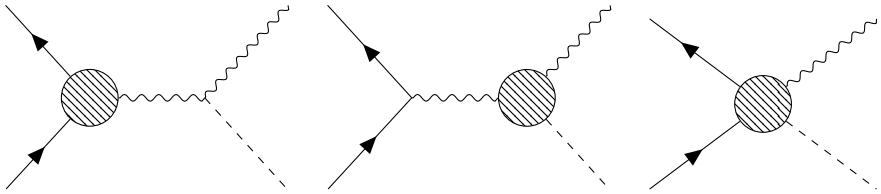

Figure 2.3: First order diagrams for SMEFT contributions to a VH process.

$\mathcal{O}_W = (D_\mu\phi)^\dagger \hat{W}^{\mu\nu} (D_\nu\phi)$	$\mathcal{O}^{(3)}_{\phi Q} = (\phi^\dagger i \overleftrightarrow{D^I_\mu} \phi) \left(\bar{q}_i \gamma^\mu \frac{\sigma^I}{2} q_j\right) \delta^{ij}$
$\mathcal{O}_B = (D_\mu\phi)^\dagger \hat{B}^{\mu\nu} (D_\nu\phi)$	$\mathcal{O}^{(1)}_{\phi Q} = (\phi^\dagger i \overleftrightarrow{D}_\mu \phi) (\bar{q}_i \gamma^\mu q_j) \delta^{ij}$
$\mathcal{O}_{WW} = \phi^\dagger \hat{W}_{\mu\nu} \hat{W}^{\mu\nu} \phi$	$\mathcal{O}_{\phi d} = (\phi^\dagger i \overleftrightarrow{D}_\mu \phi) \left(\bar{d}_i \gamma^\mu d_j\right) \delta^{ij}$
$\mathcal{O}_{BB} = \phi^\dagger \hat{B}_{\mu\nu} \hat{B}^{\mu\nu} \phi$	$\mathcal{O}_{\phi u} = (\phi^\dagger i \overleftrightarrow{D}_\mu \phi) (\bar{u}_i \gamma^\mu u_j) \delta^{ij}$

Table 2.3: Dimension-6 operators for the Higgs interaction with gauge bosons and fermions. The right column describes the fermionic interaction and the left colum the bosonic interaction.

operators. Neglecting flavour structure and Hermitian conjugation 59 new operators enter, only for dim. 6. Considering every single operator is beyond the scope of this thesis. We include only eight operators which play a role in the WH and ZH analyses. These eight operators are shown in Tab. (2.3), where they are divided into fermionic and bosonic operators. The operators are shown in the HISZ basis, used in SFitter [23]. Additionally there are three different places where SMEFT operators can enter the VH process. These diagrams are shown in Fig. (2.3), for first order contributions.

The field strengths, entering the operators for Higgs-gauge bosonic interactions, are defined as $\hat{W}_{\mu\nu} = ig\sigma^I W^I_{\mu\nu}/2$ with σ^I representing the Pauli matrices and $\hat{B}_{\mu\nu} = ig' B_{\mu\nu}/2$. The covariant derivative acting on the Higgs doublet is given by $D_\mu = \partial_\mu + ig' B_\mu/2 + ig\sigma^I W^I_\mu/2$. For the fermionic operators interacting with the Higgs, there are also Hermitian derivative terms defined as $\phi^\dagger i \overleftrightarrow{D_\mu} \phi \equiv i\phi^\dagger \left(D_\mu - \overleftarrow{D_\mu}\right) \phi$ and $\phi^\dagger i \overleftrightarrow{D^I_\mu} \phi \equiv i\phi^\dagger \left(\sigma^I D_\mu - \overleftarrow{D_\mu}\, \sigma^I\right) \phi$, where the last one appears only in $\mathcal{O}^{(3)}_{\phi Q,\, pp}$. The covariant derivative acting on the left hand side can be defined as $\phi^\dagger \overleftarrow{D_\mu}\, \phi \equiv (D_\mu\phi)^\dagger \phi$. The flavor indices in the fermionic operators are denoted by i, j.

The operators responsible for the Higgs-gauge boson interactions entering WH and ZH searches describe three-point vertices, while the fermionic operators, like $\mathcal{O}^{(3)}_{\phi Q,\, pp}, \mathcal{O}^{(1)}_{\phi Q,\, pp}, \mathcal{O}^{(1)}_{\phi d,\, pp}, \mathcal{O}^{(1)}_{\phi u,\, pp}$, describe four-point and three-point vertices. With

this different vertex structure, the fermionic operators are kinematically enhanced compared to the bosonic operators. The corresponding three-point vertices, in this case, describe an interaction between two vector bosons V and the Higgs-boson H and the four-point vertex consists of two quarks q, a vector boson V and the Higgs boson H.

3 An overview on the HVT signal

This chapter provides a short overview on the heavy vector triplet (HVT) model, which is used as a signal in the CMS ZH analysis. Going in a deeper description of the model would be too long and is not the main goal of this thesis. The description of the HVT signal is loosely based on Ref. [24].

Searching for a new heavy resonance V', which decays into a V and H boson, was the original goal of the ZH analysis in the paper of the CMS collaboration [25]. We are using this signal to check if we can reproduce the analysis which contain different kinematic cuts and selection criteria. The Feynman diagram showing the main process of the HVT signal is shown in Fig. (3.1).

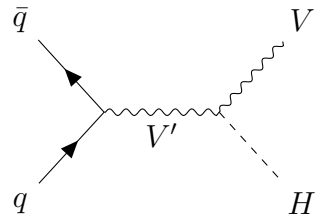

Figure 3.1: Heavy resonance V' production through $q\bar{q}$ annihilation, decaying to a V boson and a Higgs boson.

The HVT model introduces three new heavy vector bosons, one Z' and two W's. These couple to Higgs and SM gauge bosons with the parameters c_H and g_V. c_H as a parameter is in charge of the interactions between the V' bosons and the SM vector bosons V or the Higgs boson. Also c_H controls the decays of V' to bosonic channels. While g_V represents the strength of V' interactions, as a coupling constant.
The newly introduced heavy vector boson V' couples to fermions via the expression $(g^2/g_V^2)c_F$. With the coupling to fermions, the coupling constant of the $SU(2)_L$ gauge group g^2 has to be rescaled by the coupling constant of the new vector boson g_V^2. The last part of the fermion coupling is the parameter c_F. This parameter describes the direct interactions of V' with fermions. It is also responsible for the resonance production occurring with a Drell-Yan process and the fermionic decay of V'. c_F contains the overall contribution of fermions and, thus, can be split up into lepton contribution and quark contribution. The mass of the heavy vector boson is denoted with $m_{V'}$.
With this simplified model three new operators enter, namely c_{VVV}, c_{VVHH} and

c_{VHH}. But none of them contributes directly to V' decays, so they can be neglected.

HVT model is not UV complete and is usually taken as simplified model. In this case the HVT model retains only the relevant masses and couplings. This is why it is useful in resonance searches, since it is not sensitive to all free parameters of the underlying theory. It is only sensitive to those parameters, that are linked to the mass and interactions, which are either involved in the production of V' or its decay.
Because of this simplified description, it can only properly describe a narrow resonance peak. The shape of the resonance peak is well-defined by a Breit-Wigner distributions in terms of purely on-shell quantities, such as the total decay width of the resonance boson $\Gamma_{V'}$ or the product of cross section σ and Branching ratio (BR), written as $\sigma\times$ BR.

Experimentalist usually choose specific values of the parameters linked to a UV complete theory. Here, the CMS collaboration uses the minimal composite Higgs model (HCHM), with suppressed fermion couplings. For this explicit model the chosen parameter are $g_V = 3$, $c_H = -0.967$ and $c_F = 1.024$ with a resonance mass of $m_{V'} = 2$ TeV and a total decay width of $\Gamma_{V'} = 2$ GeV of the involved Z' [25].

4 Tools

This section is an introduction to the tools we used in the analysis chain. To simulate collider events, we use MADGRAPH [26, 27] for the parton level event generation, PYTHIA [28] for the parton showers and DELPHES [29] for the detector simulation. We, then, extract the EFT predictions from these events and implement it into the global analysis tool, SFitter [30].

4.1 Event simulation

We are interested in simulating collision data from LHC processes for our analysis. In order to get a data set that we can compare to the experimental data, we need to perform three steps. The first one is the event generation at parton level, the second one is hadronization and showering and lastly the detector response.

Event generation at parton level

For the event generation we are using MADGRAPH, which is a matrix element generator and a phase-space sampler. We need to provide MADGRAPH with the relevant model for our analysis in an Universal FeynRules Output (UFO) format. This UFO file contains the Lagrangian and all relevant Feynman rules with all physical parameters. It generates a matrix element, the corresponding diagrams and the helicity amplitude with ALOHA [31]. With the resulting code, the matrix element can be evaluated at a given phase space point. The Feynman diagrams for the processes are obtained by considering all possible combinations of external particles and if there are vertices in the UFO allowing the final state particle combinations, the diagram is saved in an output file.

ALOHA creates routines for helicity amplitudes to calculate the matrix element. The advantage of helicity amplitudes is that it is a convenient and effective way to compute the matrix element squared, because it works at the amplitude level, while the trace-method, which is based on completeness relations, works on a squared amplitude level. By using helicity amplitudes, the complexity grows only linearly and diagrams can be factorized. This leads to faster computations compared to the trace technique. All helicity amplitudes from every diagram can be summed and squared to yield the overall result.

The total cross section of the process is computed with the Monte Carlo integration of the squared matrix element. Because the integrals cannot be solved

analytically, it is done numerically. The phase-space points required to solve the integral are generated according to a distribution which is not exactly the real distribution describing the parton level events. To compensate this, a weight is assigned to each point, corresponding to their contribution to the real distribution. MADGRAPH then performs an unweighting procedure to turn the weighted samples into unweighted ones.
This is done by applying the standard rejection/acceptation method, also known as hit-or-miss method. In this case a random number x is extracted, which corresponds to a phase-space point. Next, the corresponding value of the function, represented by the matrix element squared in MADGRAPH, at the point x is computed. After that a random number t is extracted. If r is larger than the function value at x, a new value of x is getting sampled. This extraction of new values of x is repeated until r is smaller than the value of the function at the point x, in this case x is accepted as a value. The final distribution of the accepted values of x is equal to the true distribution of the differential cross section and each event has an equal weight [32].

Another important feature of MADGRAPH is the reweighting option, which applies corrections to the data sample that has already been generated. Starting with a generated set of events, the weights are rescaled according to

$$\omega_{new} = R \cdot \omega_{old} \quad \text{with} \quad R = \frac{|\mathcal{M}_{new}|^2}{|\mathcal{M}_{old}|^2}. \tag{4.1}$$

With this procedure we simulate contributions from Wilson coefficients needed for the SMEFT based on the data set already generated. Reweighting allows us to introduce several Wilson coefficients by using the same generated events instead of generating a new sample of events for every Wilson coefficient that is involved.

Parton showering and hadronisation

The next step in the simulation chain is PYTHIA [28], which uses the four momenta from incoming particles and simulates the parton shower and the following hadronisation.

The free partons, which consists of quarks and gluons, out of the initial process, can radiate a single gluon. These gluons can again radiate another $q\bar{q}$ pair or a gg pair, if they are highly energetic. If these quark and gluon pairs still have enough energy, they can radiate yet another quark or gluon pair and so on, as long as they have a sufficient amount of energy. At the LHC, we can see the showers induced by the processes as jets. The shower evolution in PYTHIA is based on DGLAP splitting kernels $P(z)$, describing the probability that for example a single parton will split in two with an energy fraction z. These splitting kernels $P(z)$ are derived in Ref. [15].

Then hadronisation takes place on a low-energetic non-perturbative scale. There the single partons from the showering process are grouped together in order to form hadrons. The basic principle behind hadronisation is the concept of color confinement, so only color neutral states can exist. In order to simulate hadronisation processes, a Lund string framework [33] is used in Pythia.
Color confinement can be modelled by a color flux tube, forming between particles with color. When the distance between two particles increases, the force between the particles grows linearly and the energy decreases for the color dipole. At some point the energy is too high and the color flux tube breaks and produces a new $q\bar{q}$ pair with the energy stored in the tube. The new $q\bar{q}$ pair and remaining particles can produce further $q\bar{q}$ pairs if they are highly energetic enough. At some point only on-shell particles can be produced and the process of hadronisation stops. Unstable hadrons decay into stable hadrons, for example pions and other particles decay accordingly to the decay channels implemented in Madgraph or Pythia.
The output file of Pythia contains all the information from showering and hadronisation, including the mother and daughter particles, the four-momenta of the particles, their status (at which point in the process the particle was created), particle ID and color state. These hadrons and other remaining particles are now passed on to the detector simulation.

Delphes: detector response

Of the initial process generated with Madgraph, and after showering and hadronisation in Pythia, only final stable constituents enter the detector simulation. The detector response is simulated with Delphes [29], a simple detector simulation program, which adds smearing to the final state particles to mimic smearing effects from real detectors.

It simulates a general purpose collider detector, which is made up of an inner tracker, electromagnetic and hadronic calorimeters and a muon detector. The components are organized concentrically with a cylindric symmetry around the beam axis. Starting with the calorimeters, the electromagnetic one is responsible for measuring the energy of the electrons and photons, while the hadronic calorimeter measures the energy of the long-lived charged and neutral hadrons, such as pions. For the detector simulation the particle-flow reconstruction [29] is used, which is an approach to use the maxium amount of information from all sub-detectors to reconstruct the events properly, such that each reconstructed particle corresponds to a particle-flow track.
The final state particles propagate through the magnetic field of the inner tracker and the tracks left by charged particles are used to reconstruct their momenta. A perfect angular resolution of the particle tracks is assumed and for the norm of the transverse momentum vector smearing is added. In the Delphes settings the tracking efficiency, energy and momentum resolution can be specified. Once the particles have propagated through the tracking system, they deposit their energy in

the calorimeter cells. The granularity of these cells determine the energy resolution of the particle.
Another aspect of the event reconstruction is the jet reconstruction, which is done with the FASTJET-package [34]. It allows jet reconstruction with three different algorithms, the k_T-algorithm [35], the Cambridge/Aachen algorithm [36] or the anti-k_T algorithm [37].
Differences between these algorithms are, for example, the different starting points to reconstruct and form a jet. Cambridge/Aachen starts purely geometric, while k_T begins with the soft and anti-k_T with the hard constituents [15]. To reconstruct the 4-momentum of the jet, all shower remnants from the initial parton must be recovered. In the special case of b tagged jets, we also look for a b quark within a set radius ΔR. The final number of b tagged jets also depends on the tagging and/or mistagging efficiencies, which can be modified in the DELPHES settings.

The full detector event simulation described above can take up to a minute per event. And in the end all reconstructed particles and their 4-momenta are saved in the output file.

4.2 Global EFT analyses

The EFT analyses are performed using SFitter [30], a global SMEFT analysis tool, in order to derive constraints on Wilson coefficients. It works by sampling the likelihood of a model under investigation for a given set of measurements (for example LHC processes) using Markov chains [38].

SFitter constructs a likelihood map of the parameter space and determines the best-fit parameter point. All other points are ranked in a list of the next most likely parameter points after the best-fit point. The weighted Markov chains provide us with a representative sample of parameter points. It uses a likelihood distribution $\mathcal{L}(m)$, which depends on model parameters m. This likelihood distribution is linked to a probability distribution $p(d|m)$, with d a given set of measurements. When the input data is fixed, the relation $p(d|m) = \mathcal{L}(m)$ holds.
Markov chains are a good tool for analyses involving a large number of parameters and complex likelihoods. A Markov chain describes a sequence of points, where the acceptance of the next point is only based on the present point and not previous ones. Starting with the likelihood and a random point t in the parameter space. If the likelihood evaluated at t is larger than the likelihood at the current point c,

$$\frac{\mathcal{L}(t)}{\mathcal{L}(c)} > 1, \tag{4.2}$$

the new point t is accepted and added to the chain. Otherwise a test is needed to accept or reject the new point t.

In order to pass this test the likelihood of the point t must satisfy the relation

$$\frac{\mathcal{L}(t)}{\mathcal{L}(c)} \geq r, \tag{4.3}$$

with r a random number in the interval $[0, 1]$, but also gives it a chance to jump to lower likelihood points and map out regions of parameter space further away from the best fit point. This algorithm forces the Markov chain to primarily choose points with higher likelihoods.
The performance of the Markov chain can be improved by replacing the flat probability distribution, which selects t, with a Breit-Wigner or Gaussian distribution. These distributions will select the next point, with an increased probability, around the current point c. If the current point has a high likelihood, there is a chance that points around it also have a high likelihood. Choosing a Gaussian or Breit-Wigner distribution is motivated by the continuous shape of the underlying likelihood map.

To improve the Markov chains even further a so-called burn-in phase is introduced before starting with the actual Markov chain. This helps when the starting point of the Markov chain is far off the actual best-fit region. Because then the chain can not easily reach the best fit region and the values of the likelihood are rather low compared to the best-fit values. This effect would vanish, if infinitely many points were sampled, but this is not realistic.
To avoid the computational costs which comes with very long Markov chains, a shorter Markov chain is sampled, a so called burn-in Markov chain, before the actual Markov chain. This burn-in chain contains a small number of points and it's only purpose is to find the best starting point. For chains with $N > 100$ elements in SFitter, the burn-in chain contains $N/100$ events. To extract parameter bounds from the Markov chain points sampled, we profile or marginalize over all dimensions except the one we are interested in. This so called profile or marginal likelihood is then used to extract the 68% or 95% CL intervals. This sums up the technical side of SFitter, we can start to implement new measurements.

In order to implement these new measurements, we have to insert the model and data inputs into the corresponding cards. In the model card, one can specify the settings of the fitting method. These can be, for example, the tools and computational scripts used to evaluate the SMEFT prediction at a given model point. Furthermore, all the details of the Markov chain can be exchanged, the number of points in the chain or if the new point t should be sampled from a Gaussian or Breit-Wigner distribution. In the lower part of the model file the Wilson coefficients included are specified. The default values, which are usually set to zero, can be adapted and we can define a range to sample from for each coefficient.
The data files, on the other hand, are responsible for implementing experimental data, SM background and the difference between both in SFitter.
The implementation style used in this thesis is a bin wise implementation. The bins implemented in the data card consist of three different entries. First, there is

the experimental data, next the SM background of the process and the last entry can be used to specify uncertainties on the signal prediction. With this set up, we can sample from a likelihood including up to 20 Wilson coefficients in the Higgs sector. With the model we use, the number of dimensions is chosen, such that it includes all relevant Wilson coefficients entering the input measurements.

In order to describe the experimental results as accurately as possible, SFitter has the option to assign different types of uncertainties to each measurement. The experimental data and background can be assigned systematic, statistical and theory uncertainties, while we can only assign theory uncertainties on the signal prediction. These different uncertainties can be distributed according to three different probability distributions, Gaussian, Poissonian or flat distributions. Once all the uncertainties are implemented, SFitter can treat theory and Gaussian distributed uncertainties either as fully correlated or uncorrelated. This can be chosen for each data card separately. This variety in uncertainty treatment is one of the great advantages of SFitter compared to other tools.

Overall, SFitter performs three steps in order to provide results: first, it computes a log-likelihood map of the parameter space, including the spaces of relevant Wilson coefficients, using Markov chains. Next, it determines the best fitting point from the map and ranks the other points according to their log-likelihood values. Lastly, SFitter removes all nuisance parameters, so that we are only left with the results for the Wilson coefficients we are interested in.

The next step is to use the event generation chain in order to reproduce specific LHC measurements and add the SMEFT predictions on top. The predictions can then be implemented in SFitter and constraints for Wilson coefficients can be determined. In this thesis we do this for a WH search from ATLAS and a ZH search from CMS, see respectively chapter 5.1 and chapter 5.2.

5 High kinematic VH searches

In this chapter we present the implementation of two VH searches from LHC Run II in SFitter. The first implementations is a WH process from the ATLAS collaboration and the second one is a ZH process from the CMS collaboration. In order to see the impact of these two measurements on dimension 6 operators in the SMEFT, we need to reproduce the corresponding processes as reference and then add SMEFT contributions on top of the reproduction. Afterwards, the results are implemented in SFitter. The goal is to have a global analysis involving both measurements in the end.
A summary of the whole process for the two measurements can be found in Ref. [39], more precise in the sections 4.2 and 4.3.

5.1 WH search

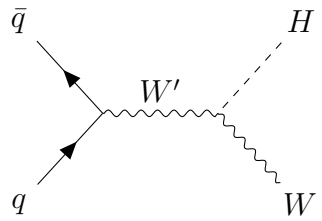

Figure 5.1: Feynman diagram for WH-production.

We start with a WH measurement from the ATLAS collaboration [40], who were originally looking for a heavy resonance, like a W', which then decays into a WH pair. The experiment did not search directly for SMEFT contributions, so we have to add them manually to the process. Nevertheless we can still use this process to constrain Wilson coefficients in SMEFT, after adding the contribution of the Wilson coefficients. Since the resonance searches involves a highly boosted Higgs boson with an invariant mass up to 4 TeV, it can even give a handle on kinematically enhanced Wilson coefficients.
Implementing these high kinematic distributions from resonance searches is not as straight forward as implementing rate and signal strength measurements. These normal measurements appear in the bulk and do not have a high kinematic tail region. Compared to them, we have different cuts and varying SMEFT contributions for kinematically enhanced Wilson coefficients.
Since this is a non-standard measurement and no EFT contribution is given in the

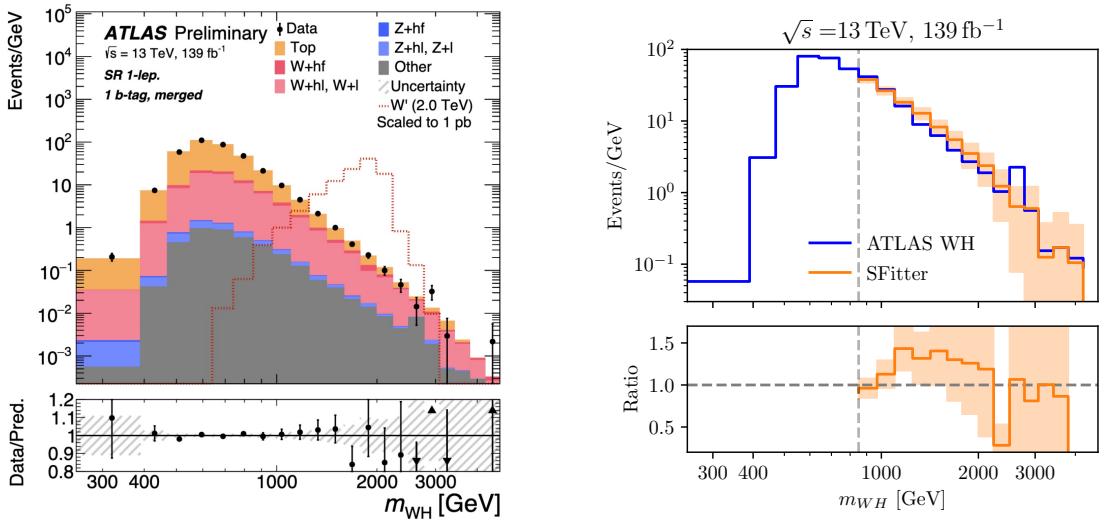

Figure 5.2: Left: measured m_{WH} distribution [40]. Right: comparison between the the ATLAS results and our SM background estimate. The orange band shows the statistical uncertainty from the Monte Carlo generation.

paper, we first need to reproduce one prediction given in the experimental paper. In this case, we choose to reproduce is a SM background. Then we will introduce a scale to match the distribution better, because we will never be able to reproduce all the cuts and detector effects with our simulation setup. Finally, we will add the EFT contribution on top of the simulated SM WH process and include these predictions inside SFitter.

The WH production process is shown in Fig. (5.1), with the W boson decaying to an $e\nu_e$ pair or a $\mu\nu_\mu$ pair and the Higgs boson H decays into a $b\bar{b}$ pair. We also choose the merged category instead of the resolved category, because the merged category reaches a higher mass region than the resolved category. In this case merged means, that both b quarks the Higgs decays into, are inside a single jet with a large radius ΔR. So the merged category contains a single b tagged jet. This is the reason why we consider the merged category, because it is easier for us to reproduce and do b-tagging with a single jet having a large radius, than with two separate smaller jets, as in the resolved category.
We are looking for a single jet with a large radius and exactly one b quark from the Higgs decay inside the jet. With this we try to reproduce the diboson and SM WH background of the process, in the left panel of Fig. (5.2) shown as the grey background labelled as 'Other'.

Background reproduction

There are five different processes involved, which contribute to the SM WH and diboson background. These processes are namely

$$pp \to W_{\ell\nu}W_{jj},\ W_{\ell\nu}Z_{jj},\ Z_{\ell\ell}W_{jj},\ Z_{\ell\ell}Z_{jj}\ W_{\ell\nu}H_{jj}. \tag{5.1}$$

Each process is generated containing 100.000 events, by using the MADGRAPH-PYTHIA-DELPHES chain. In order to reproduce these events as accurately as possible, we try to apply the same event generation and detector cuts as the ATLAS collaboration does. For this, the cuts listed in sec. 4 of Ref. [40] are used and implemented into the corresponding MADGRAPH, PYTHIA or DELPHES cards. These cuts include restrictions on the p_T of the jets and decay particles as well as restrictions on $|\eta|$. To reproduce the corresponding jets in the WH process, the anti-k_T algorithm is used in DELPHES.
Summing up the contributions from the channels contributing to the background, listed in Ref. 5.1, the reproduced background is close to the diboson background provided by the ATLAS collaboration, shown in the right panel of Fig. (5.1), but we do not completely match it. In order to improve the reproduced results to match the distribution from the ATLAS collaboration, a rescaling factor is introduced. In order to figure out this rescaling factor, the ratio between both backgrounds is taken. Therefore the background of the ATLAS group is divided by the reproduced background in each bin. To determine a global rescaling factor that can be later introduced to SFitter, the mean of the ratio is taken. This leads to a rescaling factor of 1/3.18, not including the first bins. In Fig. (5.2) we start with reproducing the background at the seventh bin. The reproduction of a high kinematic distribution is a non-standard procedure, since it is not the same as for rate measurements. For rate measurements the influence of the SMEFT is known and thus the reproduction is easier. In the reproduction of high kinematic distributions are particular cuts and driving EFT contributions included, which makes it difficult to reproduce the first bins with our simplified tools. These missing cuts in reproducing the distributions are also responsible for the small rescaling factor, which is smaller than one. In other analyses, for example the following ZH one, the reproduction factor is larger than one, coming from missing higher order corrections.
We are able to neglect the first bins, because we are mainly interested in the high-energy tail, since the EFT contributions for this process are all kinematically enhanced. Furthermore, we already have bulk measurements in SFitter constraining WH production. So the bins in the low-energy region can be removed without a huge impact on the EFT contributions.
Also the comparison between the generated events and the distribution from ATLAS shows that we find fewer events generated in the high-energy tail. Because we generate only leading order processes, without NLO and NNLO contributions. These can have a visible effect in the tail region, because of their higher order and loop contributions.
Next the bins in the distribution contributing to the reproduced background, are

re-binned in order to ensure at least two events per bin to achieve accurate statistics and a smoother distribution. After re-binning the background we are left with seven new bins, ranging from 800 to 4000 GeV.

Again, the reproduction of the background is necessary, because we look at a non-standard measurement, since it is a high kinematic distribution. Also there are no information on the EFT contributions entering the process, because this is not the main goal of the experimentalists.
So in order to get an EFT contribution that can be implemented into SFitter, we have to add it manually via the reweighting function in MADGRAPH

EFT prediction

In order to estimate the EFT contribution to the WH channel, we use the sample already simulated for this process as part of the background and we apply the reweighting tool in MADGRAPH followed by PYTHIA and DELPHES. The reweighting process assigns different values to the Wilson coefficients f_X and then reweights them based on the events generated for a given initial process, which we will also call reweighting basis. This procedure is then repeated for different combinations of the coefficients.
There are squared contributions from the coefficients, contributions from the interference with the SM or interference with other Wilson coefficients. In the WH process are three different Wilson coefficients involved, namely f_W, f_{WW} and $f_{\phi Q}^{(3)}$. This leads to ten different combinations for the Wilson coefficients and the SM.

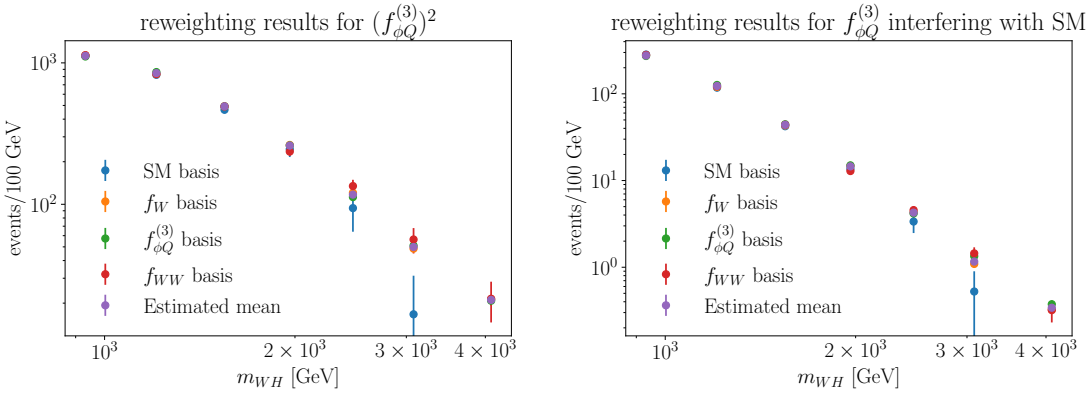

Figure 5.3: Results for the reweighting process of the quadratic contribution to $f_{\phi Q}^{(3)}$ on the left and the interference of $f_{\phi Q}^{(3)}$ with the SM in the right panel. We show the reweighting results for the different initially generated samples, which are called reweighting basis, considered and the estimated mean value with a log-likelihood approach.

The reweighting as a procedure in MADGRAPH, can be done on every generated sample. With previous implementations, we saw that the results from the reweighting can fluctuate depending on the generated sample we start with. In order to minimise these fluctuations we use different samples, meaning that we start each time from a different generated sample, to get stable results for the involved Wilson coefficients f_X. This procedure is still better than not using the reweighting procedure. Because otherwise we need to generate ten samples which are not able to reproduce the SMEFT polynomial exactly. In the case of reweighting, the SMEFT polynomial is always, making reweighting more efficient.

We are starting with the SM as initial event generation for the reweighting process, adding the SMEFT contribution on top. In order to take care of the fluctuations, the reweighting is repeated with f_W as initial event generation. Next, also the other two coefficients involved, f_{WW} and $f_{\phi Q}^{(3)}$ are used for initial event generation to minimise the impact of fluctuations on the results.
With each initial event generation, $100,000$ new events are generated. The SM as initial event generation has lower statistics and fewer events in the tail region compared to the distribution from the other reweighting bases. This comparison between the different reweighting bases is also shown in Fig. (5.3). In the 5th and 6th bin the reweighting process with the SM does not perform as good as using the other coefficients as initial event generation. With this in mind we remove the events sampled with the SM and only consider the f_W, f_{WW} and $f_{\phi Q}^{(3)}$ processes for further simulations and calculations. The purple dots visualize the estimated mean from f_W, f_{WW} and $f_{\phi Q}^{(3)}$ used as initial event generations, based on Eq. (5.4) and the uncertainty of the mean value is calculated as a weighted standard deviation as derived in Eq. (5.5). In what follows, we explain the derivation of these formulae.

We end up with three different reweighting results that needed to be combined into one data point per bin in order to be able to implement them into SFitter.
After pointing out the need to combine the reweighting results from the different bases into one, we continue by calculating the mean value for every bin containing the different reweighting results. For this we use a log-likelihood approach that is maximised in order to receive the mean value μ. In this log-likelihood approach all values are considered to be gaussian distributed and thus it can be written in the following way

$$\log(L) = \log(G_1(d_1|\mu,\sigma_1)) + \log(G_2(d_2|\mu,\sigma_2)) + \log(G_3(d_3|\mu,\sigma_3)), \tag{5.2}$$

with μ the overall mean and d_i the different datasets from the different reweighting bases and σ_i their corresponding uncertainties. In order to evaluate μ, the log-likelihood $\log(L)$ is maximised with

$$\frac{\partial \log(L)}{\partial \mu} \stackrel{!}{=} 0. \tag{5.3}$$

After taking the derivative and some calculations, the final expression for the mean value μ is

$$\mu = \frac{1}{\sigma_1^2\sigma_2^2 + \sigma_1^2\sigma_3^2 + \sigma_3^2\sigma_2^2} \left(\sigma_1^2\sigma_2^2 d_3 + \sigma_1^2\sigma_3^2 d_2 + \sigma_2^2\sigma_3^2 d_3\right). \tag{5.4}$$

In order to determine the corresponding uncertainty of μ, we are using an approach with the weighted standard deviation

$$\Delta\mu = \sqrt{\frac{a(d_1-\mu)^2 + b(d_2-\mu)^2 + c(d_3-\mu)^2}{3}}, \quad \text{with} \tag{5.5}$$
$$a = \frac{\sigma_2^2\sigma_3^2}{\sigma_1^2\sigma_2^2 + \sigma_1^2\sigma_3^2 + \sigma_3^2\sigma_2^2},\ b = \frac{\sigma_1^2\sigma_3^2}{\sigma_1^2\sigma_2^2 + \sigma_1^2\sigma_3^2 + \sigma_3^2\sigma_2^2} \quad \text{and}$$
$$c = \frac{\sigma_1^2\sigma_2^2}{\sigma_1^2\sigma_2^2 + \sigma_1^2\sigma_3^2 + \sigma_3^2\sigma_2^2}.$$

We remain with one uncertainty per SMEFT contribution entering the implementation. In order to implement them in SFitter, we need to put them together in a way that makes sense. For this we add them in quadrature, which is a good procedure as previous implementations have shown.
These values are written in so called index tables, which are read by the 'GetPrediction' function. This function the calculates based on the data, background and Wilson coefficient values the SMEFT prediction per bin.
This prediction calculated by the 'GetPrediction' function, is then used in SFitter for the analysis of the measurement. In order to get this prediction, the values for the Wilson coefficients are added on top of the SM background from the distribution, which is also part of the index tables, to make the calculation faster and easier. The sum over all the values of the Wilson coefficients are multiplied by the scaling factor extracted from the reproduction of the VV/VH SM background. To insert the values of the corresponding Wilson coefficients into SFitter, the index tables are important. In there is for each coefficient and its interference with itself, the SM or other coefficients a value saved. These values are extracted from the reweighting process. So the variables for the coefficients used in the program are multiplied with the numbers extracted from the reweighting. For the quadratic or interference terms with other coefficients, the variables are multiplied with the corresponding entry in the index table. In the end the whole 'GetPrediction'-function is multiplied by the luminosity. With this output SFitter can calculate the EFT prediction with different data and model cards.
Other things we need for a successful implementation in SFitter are the corresponding model data cards. Some details on the modification of these cards are provided in the following paragraphs.

Measurement implementation

Next we need to implement the values of the data points from the ATLAS distribution with their corresponding uncertainties in the data card of SFitter. Another part of the data card is the overall background contribution and the systematic, statistical and theory uncertainties from the measured events of the ATLAS collaboration, which all can be added in the data card. The data points and total background is taken from the left panel in Fig. (5.2) and the uncertainties are listed in sec. 7 of [40].
The uncertainties are split into systematic, statistical and theory uncertainties and can be sort into different groups. First they can have impact on the data, the background or the signal of the distribution and second SFitter has its own categories of systematic uncertainties. Some of these systematic uncertainty categories are detector, b tagging or luminosity uncertainties. Further categories are uncertainties on photon and lepton reconstruction or lepton isolation. A complete overview with the different uncertainty categories and their corresponding values given by the ATLAS collaboration is shown in Tab. (5.1). Without further informations, the uncertainties are applied on the data and background points. The theory uncertainties, coming from the SMEFT contributions, only act on the signal, which is classified by the background subtracted from the data. Usually there are no theory uncertainties from the SMEFT prediction on the data and background. Here the systematic and statistical uncertainties are considered as gaussian distributed while the theory uncertainties are considered as flat.

category	value [%]
luminosity	1.70
detector	8.25
lepton reconstruction	7.31
b-tagging	2.00
lepton isolation	5.00
statistic	14.00
theory (signal)	8.66

Table 5.1: Overview with the uncertainties given by the ATLAS collaboration. They are grouped together in the SFitter categories, where the first 5 values are all systematic uncertainties, split up in different sub-groups.

The model card contains various technical details for the Markov chains and the simulation as well as details on the involved Wilson coefficients. For example the number of sampled points can be changed or the stepsize of the Markov chain. Next, some needed SM variables are defined, such as the mass of the Higgs boson or the bottom quark and different coupling constants, like G_F or α_S. Also the different Wilson coefficients involved in the corresponding process are listed in the model card. There the starting point for the chain can be defined and the range,

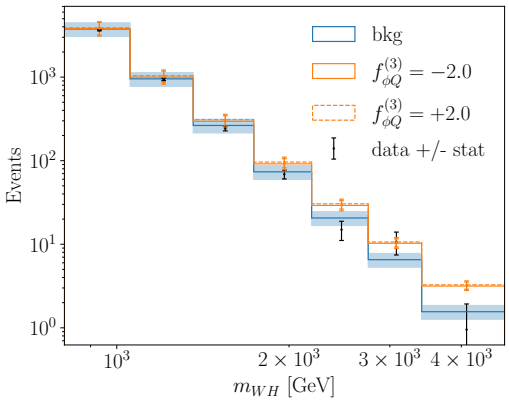

Figure 5.4: Re-binned m_{WH} distribution implemented in SFitter, including statistical and systematic uncertainties. We show the complete background and the effect of a finite Wilson coefficient $f_{\phi Q}^{(3)}$.

in which the points should be sampled. For each coefficient one can assign an individual step size in order to sample them as accurate as possible.

Now all necessary informations are implemented in SFitter and we can start with the simulations and evaluate the results. SFitter provides the impact of every coefficient individually, taking quadratic and interference terms into account. These results can be compared to the data and background distributions to see the impact of the Wilson coefficients and be able to see how constrained they are.

Leading bins and other technical details

The biggest visible pull in Fig. (5.4) between the EFT prediction made for $f_{\phi Q}^{(3)}$ and the data points in the 4th and 5th bin of the distribution. But are these bins actually the leading bins of $f_{\phi Q}^{(3)}$? In order to answer this question, one has to make an analysis with SFitter by only taking $f_{\phi Q}^{(3)}$ into account. The next step is to consider only a single bin per simulation. These results can be seen in the left panel of Fig. (5.5), comparing the single bin analyses with the one including all bins of the implemented measurement. The limits on the y-axis of the figure are shown in terms of the Gaussian equivalent

$$\Delta\chi^2 = \chi^2 - \chi^2_{\text{min}} = -2\log\mathcal{L} + 2\log\mathcal{L}_{\text{max}} \,. \tag{5.6}$$

So the leading bins for $f_{\phi Q}^{(3)}$ are the 4th and 5th bin, matching with the bins showing the strongest visible pull.

Since the theory uncertainty of the EFT prediction is an estimate, it is useful to make some further checks on the impact of theory uncertainties and their correlations. These analyses are shown in the central plot of Fig. (5.5).

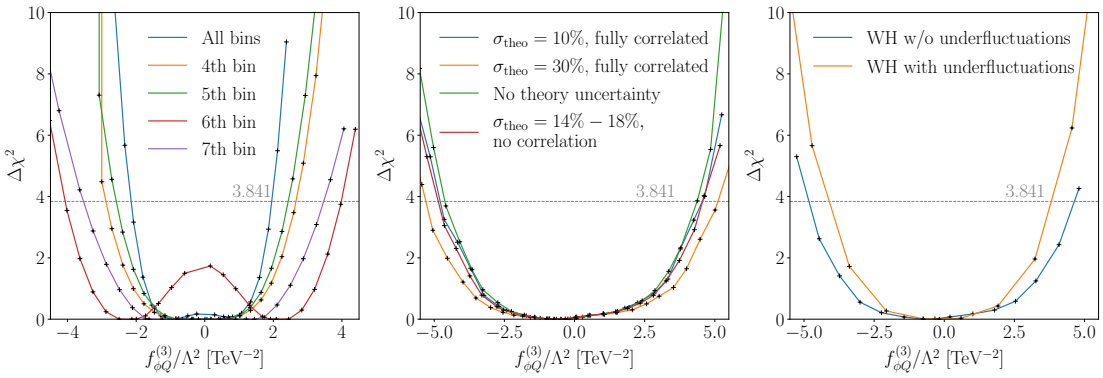

Figure 5.5: Log-likelihood for a 3-parameter analysis of the WH search as a function of $f_{\phi Q}^{(3)}$. We vary the number of bins included with uncorrelated theory uncertainties for a 1-dimensional analysis (left), the theory uncertainties and their correlation (center), and the treatment of under-fluctuations (right).

The estimated mean value of every bin is computed with a log-likelihood approach, so the theory uncertainties differ from bin to bin. They go from roughly 14% up to 18% and we assume no correlation. These results are also indicated by the red line in Fig. (5.5). To see the impact of the theory uncertainties, we are now choosing values lower than 14% and larger than 18%. For the lower end a theory uncertainty of 10% is chosen while complete correlation is assumed. This is shown with the blue line. For the upper value a 30% theory uncertainty is selected, again fully correlated and represented by the orange line. Another interesting case is to do the simulation without any theory uncertainty at all. This is represented by the green line, with a theory uncertainty of 0% and completely uncorrelated. There is no large difference between the different uncertainty tests. The results for the 30% theory uncertainty is slightly less constraining than the other ones. As expected the simulation without any theory uncertainty is the most constraining, but they are in a similar range. These results justify the selection of the weighted standard deviation procedure to estimate the theory uncertainties of the EFT prediction and implementing them in SFitter.
It also shows, that we are allowed to treat theoretical uncertainties, which are flat, as uncorrelated without any negative consequences or impact on the result compared to correlated theory uncertainties. A reason for this is, that few bins dominate the implementation. The constrains do not usually come from many bins, that all have the same strength of the pull, rather than one or two dominating bins.

Another interesting effect, which could have an impact on the contraining power of the data set, is the treatment of underfluctuations. Fig. (5.4) shows, that in the distribution of the WH process four bins display an underfluctuation. This means that the corresponding data point in that specific bin has a smaller value than the

background in the same bin.
In fact, underfluctuations are allowed by SMEFT and thus should be considered as such. Underfluctuations could even be useful appearing in the tail of the distribution. This leads to constraints on Wilson coefficients, since the data is smaller than expected.
SFitter has two different methods to treat underfluctuations. The first one is, that the signal is set to zero, if an underfluctuation occurs, where the signal s consists of the data d in that bin subtracted from the background b, namely $s = d - b$.
The second possibility is to treat underfluctuations and to allow a negative signal. Instead of setting the signal to zero when $b > d$, the signal is computed and a negative signal is allowed. For the WH analysis the underfluctuation treatment is important, since four out of seven bins include underfluctuations.

The results for both underfluctuation treatments is shown in the right panel of Fig. (5.5). There the blue line, labelled as WH without underfluctuations describes the first method with setting $s = 0$. The orange line on the other hand allows underfluctuations and thus a negative signal. Comparing the impact on the results of these two treatments shows that the results allowing $s < 0$ is more restrictive than the other one. Comparing it to the impact of the theory uncertainties, a proper treatment of the underfluctuations can constrain the Wilson coefficients even further, while a conservative treatment of theory uncetainties has the opposite effect, with loosen the constraints. So it is worth the time to think a bit about involved underfluctuations and how many bins are affected. If there are bins with underfluctutations involved, one should choose the proper underfluctuation treatment, taking a negative signal into account. With this treatment the constraining power of the distribution can be improved.

There is an old version of this WH ATLAS analysis at a lower luminosity implemented in SFitter from 2018, as shown in [41]. Thus it would be interesting to see, if the new analysis from Run II in 2022 has more constraining power and impact than the old analysis.
In order to make both analyses comparable, we take the data from the older WH analysis and perform an analysis for the three coefficients under study f_W, f_{WW} and $f_{\phi Q}^{(3)}$. This way we can compare both implementations. With this adaption both processes are comparable and can be simulated with SFitter. The results for both 3D simulations are shown in Fig. (5.6), with f_W displayed in the left panel, f_{WW} in the center one and $f_{\phi Q}^{(3)}$ in the right panel.

The results from the newer WH implementation are not more constraining than the older WH analysis from Ref. [42]. There are several reasons for this. First, the old implementation has a lower luminosity of 36.1 fb^{-1} compared to a luminosity of 139 fb^{-1}. Also the new WH analysis is implemented in a different way in SFitter. Here we use the reweighting function in MADGRAPH, which provides

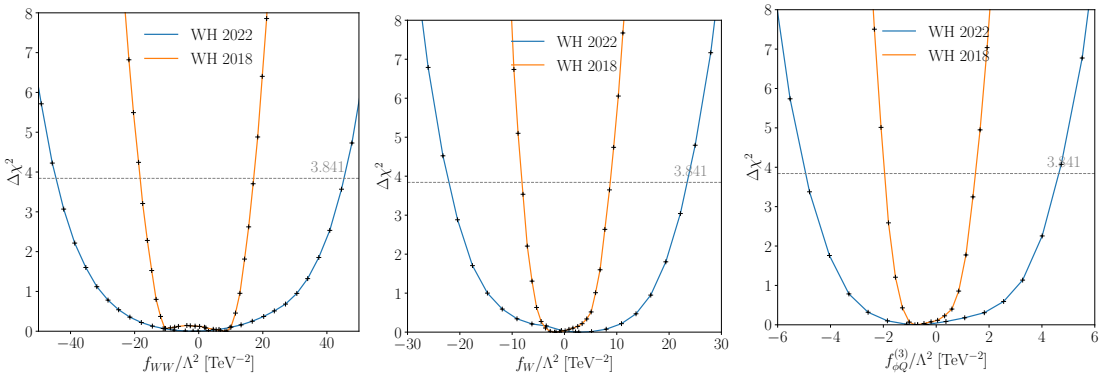

Figure 5.6: Comparison of the two ATLAS WH measurements for f_{WW} (left), f_W (center) and $f_{\phi Q}^{(3)}$ (right). The results from the 2018 implementation are shown in orange, while the 2022 results are indicated by the blue line.

us with more stable results for the SMEFT contribution. This improved procedure gives us a good handle on the theory uncertainties of the SMEFT prediction. For the previous implementation, the uncertainites on the SMEFT predicition were not considered with such an accuracy. Because the results are newer, there are more uncertainties coming from the experimental side, that have to be included. With this uncertainty treatment the newer implementation is much more conservative, but has less constraining power. But now we are able to claim the implementation as conservative, because of this precise uncertainty treatment.

We started with WH analysis from the ATLAS detector initially intended for heavy resonance searches. This WH process can also be used to constrain new physics in a SMEFT framework, since the invariant mass scale goes up to $m_{WH} = 4000$ GeV. There are good chances, that one can see an impact from kinematically enhanced Wilson coefficients, like $f_{\phi Q}^{(3)}$ in this high invariant mass regions. But in order to see an impact on these Wilson coefficients, one has to add an EFT contribution on the SM WH background of the distribution. This has to be done, because it is not a standard measurement we include in SFitter, since it is a resonance search with a high kinematic distribution. Also most experimentalists are not interested in SMEFT contributions involved in measurements, so these contributions are missing in the experimental data. After adding the EFT contribution via reweighting in MADGRAPH and adding a scaling factor to match the distribution from the ATLAS group, we are able to implement this in SFitter. The results from the new implemented measurements are not more constraining but have other great advantages. Because there are significant differences in the implementation. The reweighting process with MADGRAPH is included to provide more stable results and with this we have a better handle on theory uncertainties of the SMEFT contribution. And other uncertainties from the experimentalist side are included. Thus, the new implementation is much more conservative in terms of uncertainties, but with less

constraining power.

In the end, we are adding one more data set to the global analysis in SFitter and have a larger variety of data we can rely on. In what follows, we continue with a second measurement implement in SFitter. This time not a process from the ATLAS detector, but from CMS. It is again a VH process, but this time we choose a ZH process from the CMS collaboration.

5.2 ZH search

The next process we consider is a ZH process from the CMS collaboration, as shown in Ref. [25]. Again, this measurement was originally used to search for a heavy resonance Z', for the previous WH process. This heavy resonance Z' should then decay into a ZH pair. Since this is again a non-standard measurement and no EFT contribution is provided from the paper, we first have to reproduce one predicition given in the paper, in this case it is the HVT signal. Then we have to introduce a scale to match the experimental distribution, because we are not able to reproduce all the cuts and detector effects accurately with our simpler simulation setup. Finally the scaling factor is applied on the ZH background reproduced in MADGRAPH and we can add the EFT contribution on top and include all these predictions in SFitter. The measurement is valuable to constrain Wilson coefficients, since it involves a highly boosted Higgs boson with a mass distribution up to 2.2 TeV. This should allow it to better constrain kinematically enhanced coefficients.
The experiment looks for a $q\bar{q}$ annihilation to produce the heavy resonance Z', which then decays into a Z boson and a Higgs boson H. The full process is shown in Fig. (5.7) and is considered as an associate production process and not as VBF. Later the Z decays into a l^-l^+ pair, where we are only interested in the case when the lepton pair is an e^+e^- pair, and the H boson decays into a $b\bar{b}$ pair.

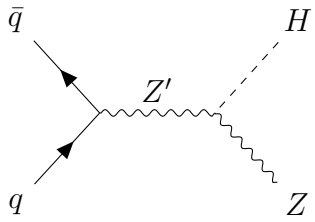

Figure 5.7: Feynman diagram for ZH-production via a heavy resonance Z' decay.

We are interested in the distributions given in the middle row of Fig. (5) in Ref. [25], where the Z has to decay into an e^+e^- pair. There is a separation between two b-tag categories and we consider both of them, the $\leq 1b$ and the $2b$ category. The Higgs boson decays in a single jet with a large radius ΔR, having the b's inside. On this single jet b-tagging is applied to. There are two possible ways to achieve results without any b-tags inside the jet. One is, that the Higgs boson is not decaying into b quarks and the other one is through the applied mis-tagging rate. Since there is a possibility, that the detector is not identifying each b quark correctly. In the end, we need to rescale the ZH distribution including the SMEFT contribution to match the experimental data. To be able to determine this rescaling factor we use the HVT signal shown for each b-category. Further information on the HVT signal can be found in chapter 3.

In order to reproduce the SM ZH process and add the SMEFT contribution manually on top, we use the MADGRAPH reweighting function together with PYTHIA and DELPHES.
To reproduce the process accurately to be able to compare it to the experimental data, the same generation cuts have to be applied. These restriction cuts implemented in MADGRAPH, PYTHIA and DELPHES can be found in section 4 and 5 of Ref. [25]. To perform jet clustering, the anti-k_T algorithm is used in DELPHES. But even with considering all these restrictions and cuts, we cannot reproduce all detector effects accurately. This is why a rescaling factor is introduced, to get rid of these artifacts. The rescaling factor is determined by comparing the reproduced results to the ones from the CMS collaboration.

HVT signal reproduction

In this process we decide to reproduce the HVT signal to determine the rescaling factor for both b categories separately. The possible signal contains the process

$$pp \to Z' \to Z_{\ell\ell} H_{bb} \,, \tag{5.7}$$

which has the advantage that there is a clear peak and it was simulated by CMS using MADGRAPH. This makes it easier to reproduce than the continuum VV/VH background. The reproduction of the HVT signal is shown in Fig. (5.8).
For event generation the MADGRAPH-PYTHIA-DELPHES chain is again used. The Z' should have a mass of $m_Z = 2000$ GeV and a decay width of 0.1% of its resonance mass. So in this case the decay width is 2 GeV. Doing only this, we still had problems reproducing the HVT signal quoted in the paper. By talking to the authors, we discovered that the reason for this, is that the signal from the CMS collaboration is normalised to 1 fb and then fitted to a Crystal Ball function. A Crystal Ball function has a Gaussian core and the tail in the low-end, after a certain threshold, is described by a power-law function.
With the normalised signal we are able to reconstruct the number of events in the signal of the CMS collaboration and in the reproduced signal. By comparing the overall number of events we are able to introduce an overall rescaling factor for both b tagging categories.

For this process using the b-tagging with DELPHES gives us results that are far off of the CMS distribution. This problem still arises after using the same b-tagging and mis-tagging rates and efficiencies. In order to match the distribution we introduced a b-counting instead of b-tagging in the detector output analysis. After that we are able to apply b-tagging efficiencies manually. This is done by multiplying the b counting results with a choosen efficiency for the b-tagging. The new b-tagging efficiency is 85% instead of 75% and the mis-tagging rate stays the same as in the paper with 3%.

After generating 100,000 events for the HVT signal, the corresponding cross-section for the process is 12.26 fb. To match the peak of the CMS HVT signal better, we recalibrate the detector and add a multiplicative mass shift of 1.05.
Since the CMS collaboration provides a HEP-data entry for this analysis, it is easier to compare the two distributions and get the corresponding rescaling factor. With the data for the HVT signal from HEP-data, we can sum up the number of events in the signal and compare the overall number of events from the CMS HVT signal to the overall number of events in the reproduced HVT signal. The procedure of taking the ratio between the two curves is redundant as mentioned before, since

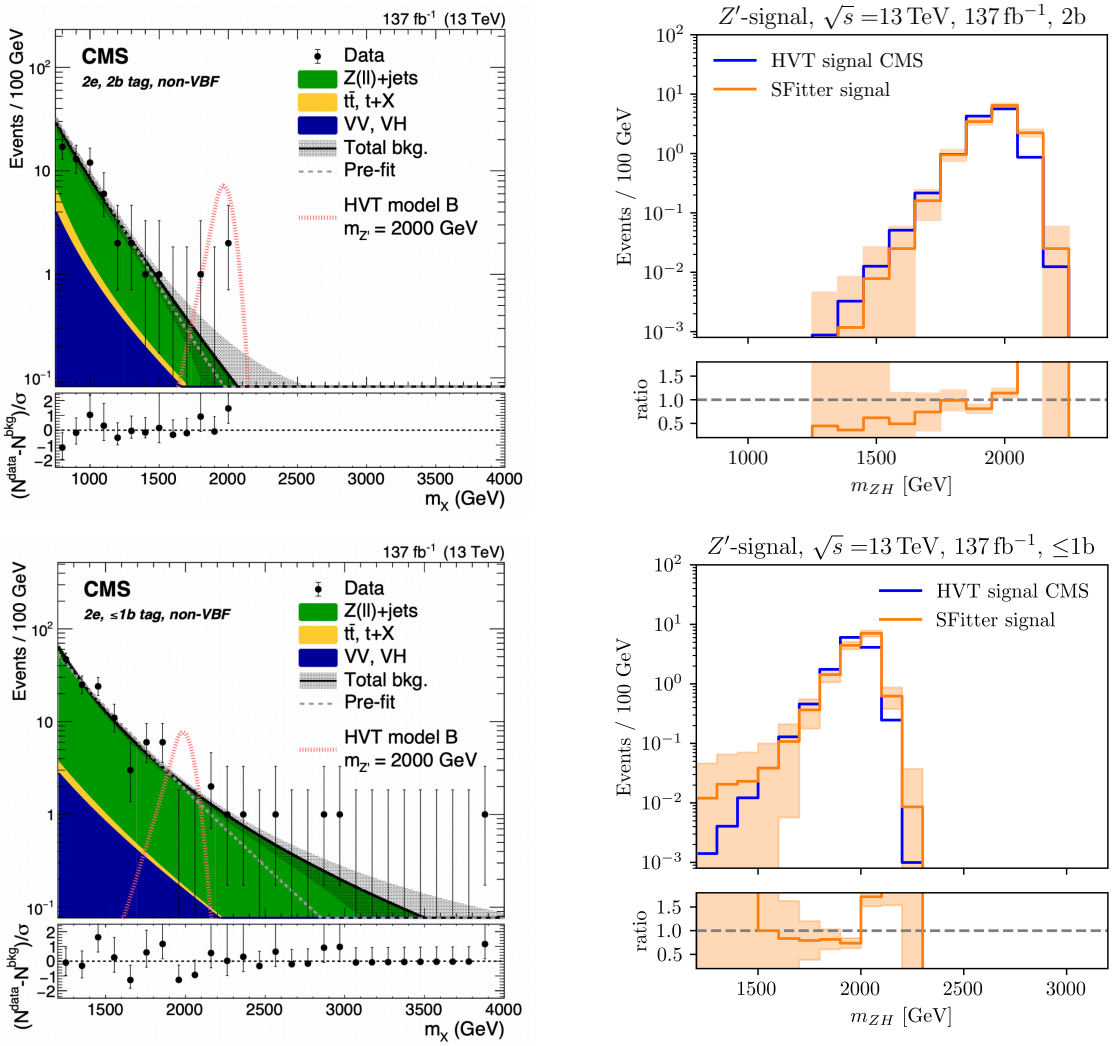

Figure 5.8: Left: measured m_{ZH} distributions for the two b-tagging categories [25]. Right: comparison between the Z' signal quoted by CMS and our estimate. The orange bands show the statistical uncertainty from the Monte Carlo generation.

both curves are normalised to 1 fb and fitted to a Crystal Ball function.
By comparing the overall number of events of both distributions, we obtain a rescaling factor for the $2b$ category of 1.14 and a factor of 1.15 for the $\leq 1b$ category. Both factors are really similar and are scaling the reproduced signal up to get closer to the one from CMS. This rescaling factor is also applied on the ZH channel to scale it up and get closer to the experimental results. Because this channel is used to generate the SMEFT contribution, so the rescaling factor also has been applied on the prediction function in SFitter.
To gain better statistics we need to re-bin the distribution to ensure that the new bins contain at least two events per bin. With this goal the distribution is re-binned into eight new bins, ranging from 1200 GeV up to 4000 GeV for the $\leq 1b$ category and from 700 GeV to 2100 GeV for the $2b$ category. We exclude bins in the high energy region containing no events for both categories, this ensures better statistics and a smoother distribution.

EFT prediction

The SMEFT contributions for this process are added on top of the SM ZH background, which is generated with the following process

$$pp \to ZH \to e^+e^- \, b\bar{b} \, . \tag{5.8}$$

After generating the background we use the same procedure as in Sec. 5.1 to add the SMEFT contribution with the MADGRAPH reweighting function. For this process eight different Wilson coefficients enter, instead of only three as in the WH process. These coefficients are namely f_W, f_{WW}, f_B, f_{BB}, $f_{\phi Q}^{(1)}$, $f_{\phi Q}^{(3)}$, $f_{\phi u}^{(1)}$ and $f_{\phi d}^{(1)}$.
To gain more stable results from the reweighting procedure, we use again different coefficients for the initial event generation, also called rewighting basis. For this ZH process we use f_W, $f_{\phi Q}^{(1)}$, $f_{\phi Q}^{(3)}$, $f_{\phi u}^{(1)}$ and $f_{\phi d}^{(1)}$ additionally to the SM for initial event generation. The coefficients $f_{\phi Q}^{(1)}$, $f_{\phi Q}^{(3)}$, $f_{\phi u}^{(1)}$ and $f_{\phi d}^{(1)}$ are kinematically enhanced in the high energy region and thus provide more stable results than f_W or the SM. With this we can neglect the f_W and SM as reweighting bases and in the following only consider the other coefficients.
Next, the different approaches for event generation are compared to find the ones with good results for each of the two b-category. Looking at the results for the $2b$ category, the most stable generation processes, with good agreements, are $f_{\phi Q}^{(3)}$, $f_{\phi u}^{(1)}$ and $f_{\phi Q}^{(1)}$. On the other hand for the $\leq 1b$ category, there are good agreements in the initial event generation of $f_{\phi d}^{(1)}$, $f_{\phi Q}^{(1)}$ and $f_{\phi Q}^{(3)}$. There is a change from $f_{\phi u}^{(1)}$ in the $2b$ category to $f_{\phi d}^{(1)}$ in the $\leq 1b$ category. We do not know why the reweighting process works well with one of $f_{\phi d}^{(1)}$ or $f_{\phi u}^{(1)}$ and we are not able to interchange them without having unstable results. Some coefficients can cause problems in populating the high energy tail but in the end we do not understand exactly what is causing the

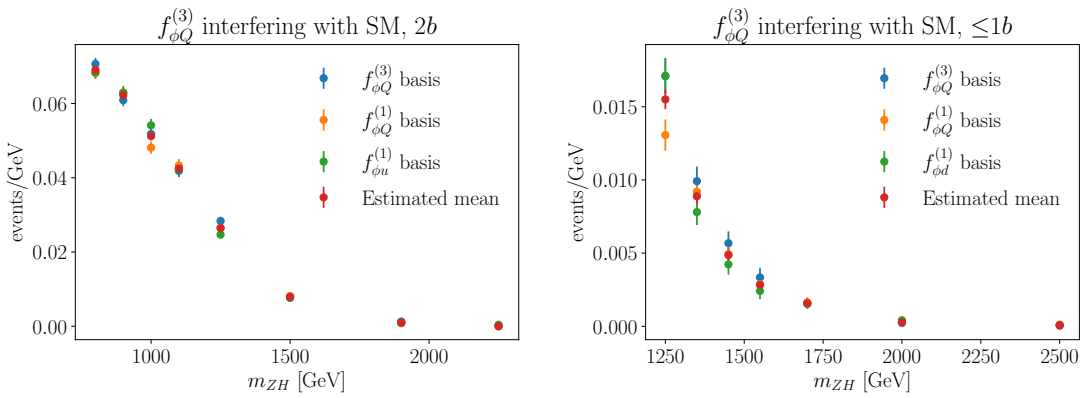

Figure 5.9: Results for the reweighting process of the interference of $f_{\phi Q}^{(3)}$ with the SM. The left side shows the results with $f_{\phi Q}^{(1)}$, $f_{\phi Q}^{(3)}$ and $f_{\phi u}^{(1)}$ as the initially generated sample, which is also called reweighting basis, for the $2b$ category and on the right side there are the results with $f_{\phi Q}^{(1)}$, $f_{\phi Q}^{(3)}$ and $f_{\phi d}^{(1)}$ as reweighting basis for the $\leq 1b$ category. The estimated mean value is computed with a log-likelihood approach.

unstable results.
The results from the reweighting process are shown in Fig.(5.9), with the $2b$ category on the left hand side and the $\leq 1b$ category on the right hand side. In these plots, only the three initial event generations are shown, which also contribute to the mean value. The mean value and its uncertainty are calculated by using Eq. (5.4) and Eq. (5.9) respectively, which are similar to the equations for the WH process. Similar to the WH process, we generate $100,000$ new events for each initial event generation.

In order to get a mean value to combine the different results from the three bases we use the log-likelihood approach again from Eq. (5.4). For this process however the uncertainty of the mean value is estimated via gaussian error propagation and not the weighted standard deviation as for the WH process. For this analysis both methods provide the same results with small deviations. Looking at the impact of theoretical uncertainties in Fig. (5.5), we can see that small variations in the theory uncertainties do not have a large impact on the constraining power of the analysis. Calculating now the uncertainty of the mean value μ with gaussian error propagation leads to the following uncertainty

$$\Delta\mu = \frac{\sigma_1\sigma_2\sigma_3}{\sqrt{\sigma_1^2\sigma_2^2 + \sigma_1^2\sigma_3^2 + \sigma_3^2\sigma_2^2}}. \tag{5.9}$$

With this uncertainty we are left with 44 uncertainties per bin from every possible coefficient and their combinations, for example f_W^2, f_W interfering with the SM or f_W interfering with f_B. To reduce them to only one uncertainty per bin, they are

category	$2b$ cat. [%]	$\leq 1b$ cat. [%]
luminosity	1.80	
detector	9.23	
lepton reconstruction	3.00	
b-tagging	6.50	0.60
lepton isolation	3.60	
statistic (bkg)	19.48	
theory (signal)	6.00	

Table 5.2: Overview of all uncertainties given for the ZH process. They are grouped together in the relevant SFitter categories, where the systematic uncertainties are split up in different sub-groups.

summed up in quadrature. The mean values for every bin and coefficient do not have to change, because they are directly implemented in the index tables used by the 'GetPrediction' function in SFitter. There every bin has its own values for the corresponding Wilson coefficients and their combinations.

Measurement implementation

Next the data and total background values for each distribution are extracted from the HEP-Data file including their corresponding uncertainties. These are implemented bin by bin in the data card of SFitter. The next step is to get the systematic, statistical and theoretical uncertainties for both categories. Statistical uncertainties for the data points are also extracted from the HEP-Data file, while the systematic and theoretical uncertainties can be found in Sec. 7, Tab. 4 of [25]. Systematic uncertainties are again split up into different categories, the same as for the WH analysis. The statistical and theoretical uncertainties can either affect the SM data, the total background or the signal prediction. So they are separately applied either on the data, background or signal prediction. For example the theoretical uncertainties from MADGRAPH on the reweighting process affect the signal and are thus only applied on the signal prediction. A full overview with all uncertainties from the ZH process implemented in SFitter is in Tab. (5.2). The first five values are all systematic and applied on data and background. Next there are statistical uncertainties only applied on the background and theory uncertainties on the signal.

Technical details and leading bins

Using all the provided data and uncertainites, the implementation into SFitter is done and first simulations can be started. The results are shown in Fig. (5.10), where the EFT contribution for the $2b$ category is shown on the left and for the

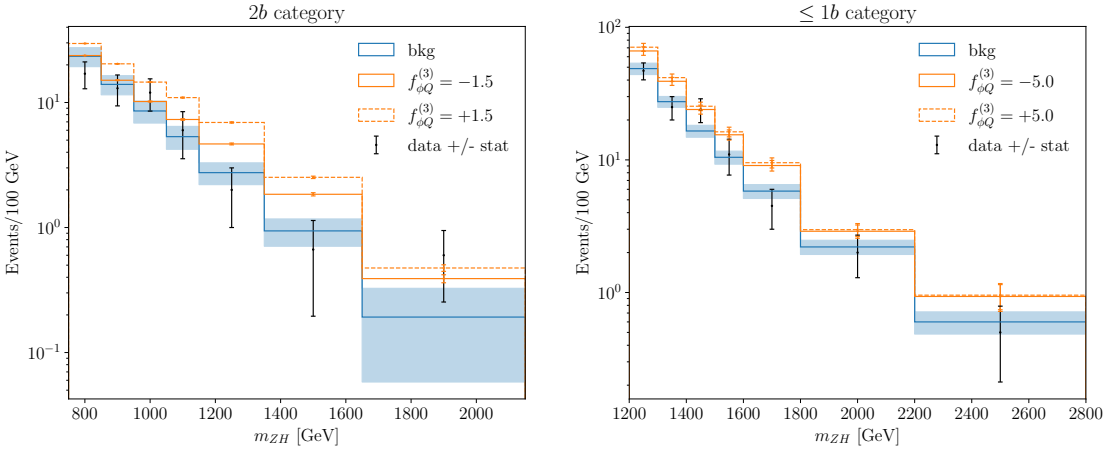

Figure 5.10: Re-binned m_{ZH} distributions for the $2b$ category (left) and the $\leq 1b$ category implemented in SFitter, including statistical and systematic uncertainties. We show the complete continuum background and the effect of a finite Wilson coefficient $f_{\phi Q}^{(3)}$.

$\leq 1b$ category on the right hand side.
Since the coefficients $f_{\phi Q}^{(3)}$, $f_{\phi Q}^{(1)}$, $f_{\phi d}^{(1)}$ and $f_{\phi u}^{(1)}$ are kinematically enhanced, they have more constraining power than f_W, f_{WW}, f_B or f_{BB}. We choose $f_{\phi Q}^{(3)}$ to compare it more easily to the WH results from the previous analysis.
The $2b$ category contains two bins, that have the biggest visible pull between the EFT prediction made for $f_{\phi Q}^{(3)}$ and the data points. These bins are the 4th and 5th bin (counting from left to right) and both of them are in a higher energy region ranging from 1200 to 1700 GeV. In this region some of the included Wilson coefficients are already kinematic enhanced.
In order to determine the leading bin for the $2b$ distribution, we consider an analysis with only $f_{\phi Q}^{(3)}$. The analysis includes one bin at a time, while the others are commented out in the data card. The result is shown in the left panel of Fig. (5.11), where the leading bins are the 4th and 5th bin, matching the bins with the strongest pull according to Fig. (5.10). Like for the previous measurement these bins are not the highest ones, but they have either an underfluctuation or are right on top of the background and they have uncertainties, that are not as high as the ones from the higher bins.

The $\leq 1b$ category has three bins providing the strongest pull between the EFT prediciton of $f_{\phi Q}^{(3)}$ and the data points. These are the 1st, 2nd and the 5th bin, which is also shown in the right part of Fig. (5.11). Again, the bins are in a higher mass region, for the first two bins between 1200 and 1400 GeV and the 5th bin is in a region around 1750 GeV. Determining the leading bins with an analysis containing only a single coefficient, we see that the leading bins are the 1st, 2nd and 5th bin, matching the expectation from Fig. (5.11).

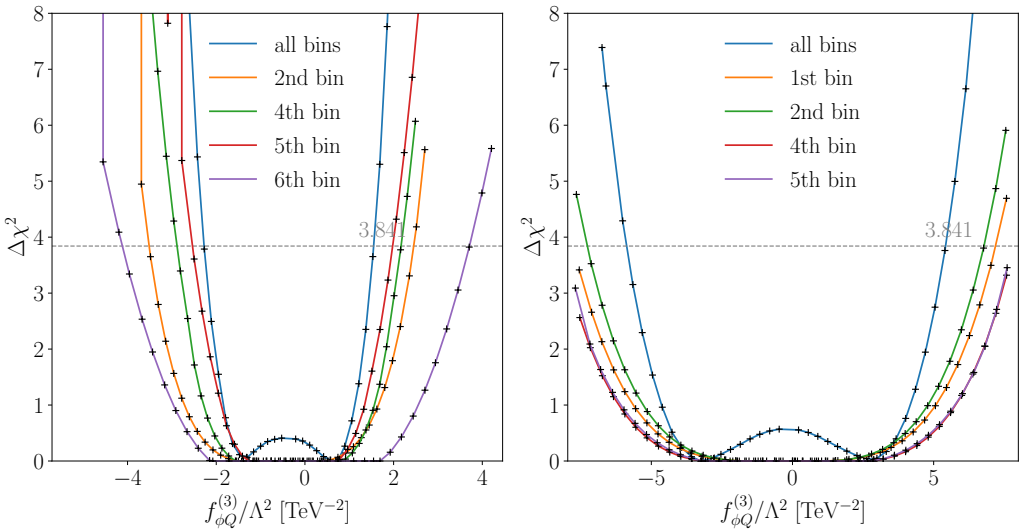

Figure 5.11: Determination of the leading bins for each b-tag category. With the $2b$ category on the left and the $\leq 1b$ category on the right side. This is done by using the coefficient $f_{\phi Q}^{(3)}$ for both categories. In this measurement we do not allow underfluctuations.

Since both of the two b categories are from the same data set and collisions, we should be able to compare them. Fig. (5.12) displays this comparison between both categories for the coefficients f_W (left) and $f_{\phi d}^{(1)}$ (right). For every coefficient the $2b$ category is far more constraining, than the results from the $\leq 1b$ category.

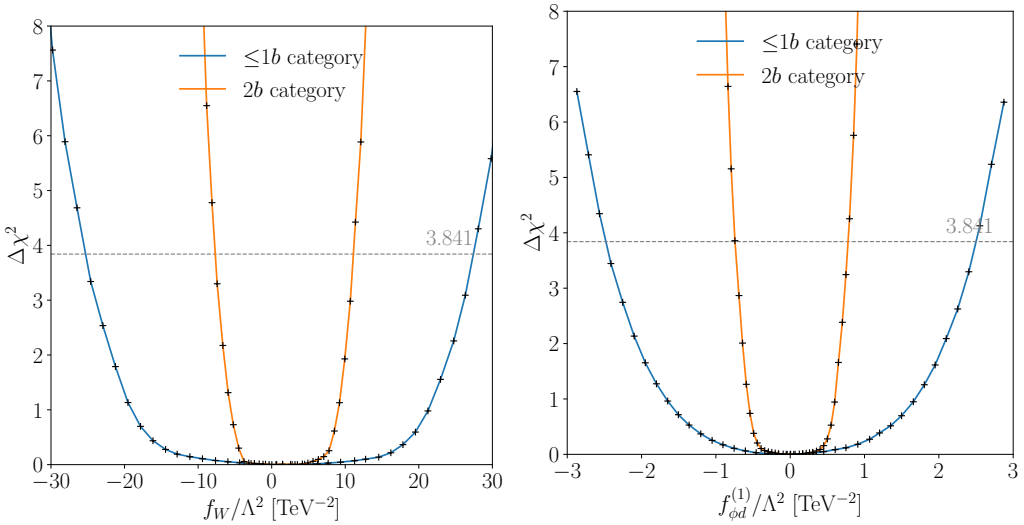

Figure 5.12: Log-likelihood for f_W (left) and $f_{\phi d}^{(1)}$ (right) with both b-tag categories. The $2b$ category is represented by the orange line and the $\leq 1b$ category by the blue one.

	2b	≤1b
data	0.667	11.0
background	0.940	10.461
data - bkg	-0.273	0.534
signal pred.	14.935	5.82
uncertainty	1.281	5.074
$\Delta\chi^2_G$	140.8078	1.074

Table 5.3: Comparing prediction values in SFitter for both b categories at $m_{ZH} = 1500$ GeV. Considering the corresponding data and background points, the signal prediction and the uncertainty on the signal prediction. The results for $2b$ are shown in the left column and the ones for $\leq 1b$ in the right one.

By just looking at the plots there are no obvious reasons for this discrepancy between both categories. One would expect that the $2b$ category is less constraining, because its mass distribution does not reach such high mass regions as the $\leq 1b$ category and has fewer events in it. So why is it then more constraining? To answer this question, we have to compare the data, signal prediction and uncertainties for both categories at roughly the same mass. We choose a region of order $m_{ZH} = 1500$ GeV. The values in Tab. (5.3) are extracted from a one dimensional fit, using only $f_{\phi Q}^{(3)}$ and for the computations we choose $f_{\phi Q}^{(3)} = 5$ as a starting point for both categories. The signal prediction for the $2b$ category is much larger than the corresponding background and data. Comparing this to the $\leq 1b$ category, there the signal prediction is more reasonable and even smaller than the corresponding data and background. Another value to check is $\Delta\chi^2_G$ which can be calculated in the following way for a Gaussian distribution

$$\Delta\chi^2_G = \frac{(d-b-s)^2}{\sigma^2_{\text{tot}}}, \tag{5.10}$$

with data d, background b, signal prediction s and the total uncertainty σ_{tot}. Comparing the results of calculating $\Delta\chi^2_G$, the outcome for $\Delta\chi^2_G$ of the $2b$ category is a factor 130 larger than $\Delta\chi^2_G$ for the $\leq 1b$ category.
A possible reason for this is, that the total background from the CMS result is implemented, including more background types than just VV/VH. But the SMEFT prediction for the Wilson coefficients is only applied on top of the ZH part from the VV/VH channel using reweighting. So the SMEFT prediction is not added on top of the whole background rather than a small fraction. The total background is larger for the $\leq 1b$ category, but the fraction of the VV/VH background is smaller compared to the $2b$ category. Taking the background ratio between the total background and VV/VH background, for the $2b$ category the VV/VH is on average responsible for 20% of the total background per bin, compared to an average of 5%

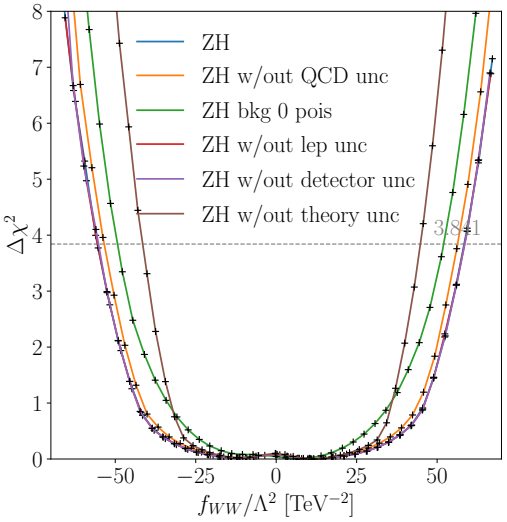

Figure 5.13: Investigating the influence of different uncertainties on the constraining power of f_{WW}. For this single uncertainty groups, like detector, theory or QCD uncertainties are removed and the result is compared to the distribution of f_{WW} including all uncertainties.

in the $\leq 1b$ category. For the $\leq 1b$ category the $Z(ll)$+jets background dominates over the VV/VH background. Another point is that the overall number of ZH events in the $2b$ category is larger, since the Higgs boson predominantly decay into b-quarks which are in one fat jet. These are possible explanations for the larger signal prediction of the $2b$ category and thus the larger constraining power compared to the $\leq 1b$ category.

It is interesting to investigate the impact of the other uncertainty categories on the constraining power of the measurement, like the systematic and statistical ones. In order to compare them, the different uncertainties are split up into different categories. First, there are systematic uncertainties on the background from QCD effects. Removing these QCD effects, we can see that they have a small impact on the constraining power, as shown in Fig. (5.13) by the orange line. Next there is a possibility to assign a poissonian distributed uncertainty on the background in SFitter. As shown with the green line, the impact of removing this is larger than the impact of removing the QCD effects. Another uncertainty category are lepton uncertainties, which are purely systematic. The effect of removing lepton uncertainties is indicated by the red line and has nearly no impact. Besides the lepton uncertainties, the detector uncertainties are also large compared to other systematic uncertainties, like the ones on luminosity or b-tagging. But the distribution does not gain more constraining power from removing detector uncertainties, as indicated by the purple line. The largest impact comes from the theory uncertainties on the signal, as shown by the brown line. In order to improve the constraining power, there should be a large improvement on theory uncertainties, not only 10%.

Because for this ZH analysis and implementation the theory uncertainties varies between 20 and 70% per bin. There are different reasons for such large theory uncertainties, for example poor statistics in various bins. In the high energy tails there are eight bins combined into one bin after re-binning, because some bins do not have any events in them, which leads to large uncertainties.

The next step is now to compare the VH measurements and then combine them into a larger dataset as a new VH implementation. These combined measurements are then compared to older implementations of VH measurements and we perform a SFitter analysis with eight Wilson coefficients involved for the new VH implementation described in this chapter.

6 SFitter global analyses

This chapter provides an overview on possible global analyses with the previously implemented WH and ZH measurements, that are introduced in chapter 5. We start with a comparison between both measurements involving the three coefficients, that are involved in both processes. Next, the two analyses are combined into an overall VH measurement with one corresponding model and data card. This makes a comparison between the new VH analysis and older ones possible and easier. For the older analysis we consider the VH measurements implemented in 2018 from early Run II results and two newer VH implementations from later Run II results in 2021.

Comparing the WH and ZH implementation

We start with a comparison of the WH and ZH process with the corresponding Wilson coefficients they have in common. Since the ZH analysis from CMS includes eight coefficients but the WH ATLAS analysis contains only three coefficients, we reduce ZH to three coefficients. These are the same Wilson coefficients as involved in the WH implementation.

Also we combine both measurements of the two b categories entering the ZH process into one measurement. Instead of two different measurements for the ZH implementation, we are left with a single one and compare this to the result from

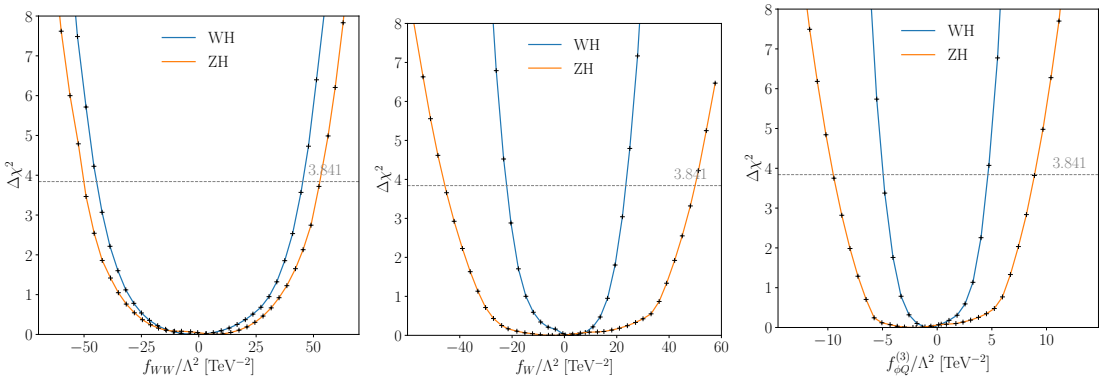

Figure 6.1: WH and ZH implementation for three coefficients, f_{WW} (left), f_W (center) and $f_{\phi Q}^{(3)}$ (right). The blue line indicates WH and the orange one ZH.

the ATLAS WH process. This comparison of the two measurements is shown in Fig. (6.1), for a simultaneous analysis of three coefficients f_W in the left part, f_{WW} in the center and $f_{\phi Q}^{(3)}$ on the right. CMS ZH is indicated by the blue lines and ATLAS WH results by the orange ones.
As shown the results for WH are more constraining than the ZH results for all three coefficients. Even though the ZH analysis contains more bins and thus provides more data points for the analysis. A possible explanation for this could be smaller error bars on the data points and EFT prediction for the WH analysis compared to the ZH. Also the WH measurement reaches a higher invariant mass up to 4 TeV, while the largest invariant mass in the $2b$ category is around 2.1 TeV and around 2.8 TeV for the $\leq 1b$ category.

Even if ZH is not as constraining, it takes more Wilson coefficients into account. This is good, because we are not only looking for the constraining power of the processes but also for correlations between the different coefficients in a global SMEFT analysis. For correlation the ZH has an advantage because it involves more coefficients. Thus it can show correlations between and with coefficients that are not included in the WH process.

Global analysis with the high kinematic VH measurements of 2022

After looking at both measurements separately and comparing them, the next step would be to combine both ZH implementations with the WH process into a single

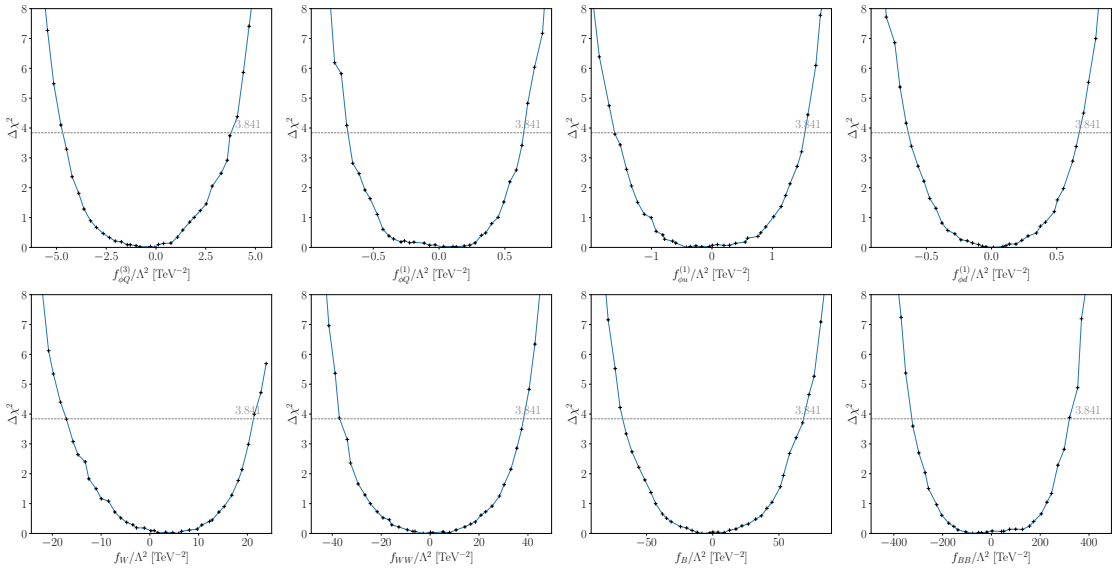

Figure 6.2: Log-likelihood for all eight coefficients entering the new VH implementation. The upper row shows the coefficients entering in fermionic operators and the lower row the ones entering in bosonic operators.

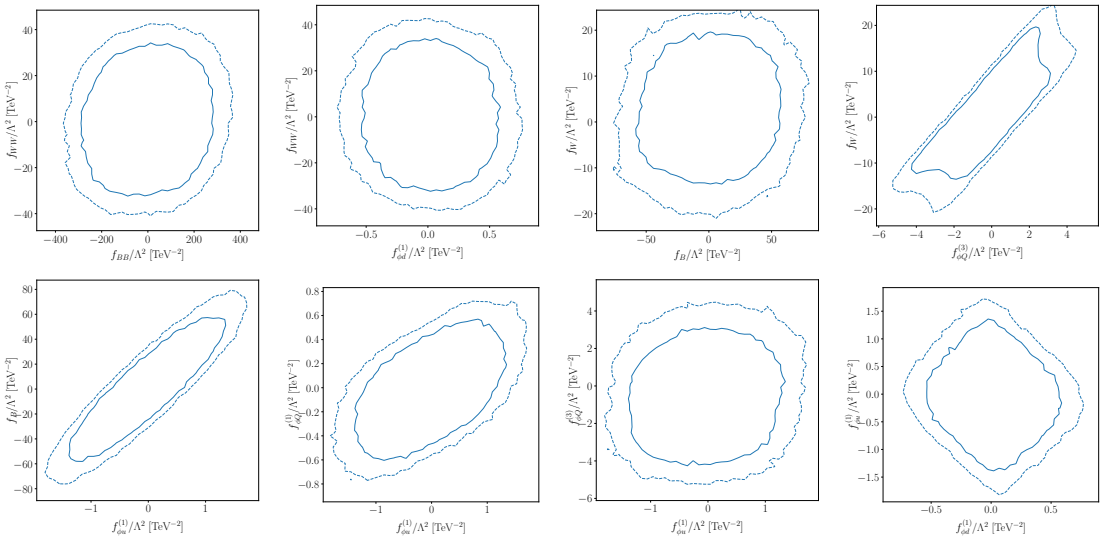

Figure 6.3: Correlation plots for various pairs of coefficients based on the VH 2022 implementation.

VH implementation. Therefore one data card is created with all three measurements, both from CMS and the one from ATLAS. The model card for the combined measurement now includes all eight Wilson coefficients involved in the ZH process. Overall the combination of the processes from ZH and WH provide a data card containing 21 bins, going up to a mass region of 4000 GeV and have an impact on eight Wilson coefficients. With this increased number of bins involved in the VH analysis, we can gain more statistics and provide results for an eight dimensional analysis using the SFitter framework. The results for these analysis with the VH processes from 2022 are shown in Fig. (6.2). In the upper row the four fermionic coefficients are shown. Namely from left to right: $f_{\phi Q}^{(3)}$, $f_{\phi Q}^{(1)}$, $f_{\phi u}^{(1)}$ and $f_{\phi d}^{(1)}$. The lower row displays the remaining four coefficients, responsible for bosonic interactions, namely f_W, f_{WW}, f_B and f_{BB}.

Looking at the results, they provide us with a stable distribution for a global analysis. This is not necessarily expected, since there are eight coefficients involved in the measurement by using only 21 bins. And only three out of the eight coefficients play a role in all of the 21 bins, $f_{\phi Q}^{(3)}$, f_W and f_{WW}, because these are the only ones, that are also constrained by the WH process from ATLAS. The other five coefficients are only constrained by the 14 bins from the ZH measurement.
Next, we have a look at the correlations between various coefficients involved in the global analysis. For this two dimensional contour plots are used. Some of the results are shown in Fig. (6.3).

Not only the constraints on single Wilson coefficients are important, we also have to look at possible correlations between the coefficients involved. This is useful to

figure out a possible relation between single coefficients, which are influencing each other. A positive correlation is shown by a diagonal shape from the bottom left to the top right corner, while a negative correlation is represented by a diagonal line from the top left to the bottom right corner. The closer the 2-dimensional contour plots are to this diagonal lines, the stronger the correlation between the two coefficients shown.
A good example for a positive correlation is between f_B and $f_{\phi u}^{(1)}$ in the left plot in the lower row. Another example for a positive correlation is shown in the right plot in the upper row involving f_W and $f_{\phi Q}^{(3)}$. If there is no or nearly no correlation between two coefficients, the shape looks like a circle. This can be seen in the second left plot in the upper row with f_{WW} and $f_{\phi d}^{(1)}$ involved. The shape is close to a circle and thus there is no correlation between these two coefficients. Other shapes, between a circle or the previously described diagonal lines are in between no correlation and fully correlated.
But for a truly global analysis more measurements and coefficients are needed and should be added to get a better overview of the correlations between different coefficients and to get a better handle on their constraining power.

With this results, the global analysis of the VH results can be compared to global fits involving older VH measurements. For example there are VH measurements implemented from 2018 and 2021, but these are all processes from the ATLAS collaboration and no CMS measurement is included. The next step is to have a look if the newly implemented VH results are more constraining than the older ones and which measurements are the leading ones for the VH processes.

Global analysis of high kinematic distributions

The older high kinematic implementations contain measurements from 2021 and 2018, which are all from the ATLAS collaboration. These measurements from 2021 are a WH measurement from Ref. [43] and a WW measurement from Ref. [44]. Also the two measurements from 2018 involve a ZH measurement taken from [45] and the other one is again a WH process from [42]. The overall goal is to replace the older 2018 WH measurement with the new one from 2022, because the newly implemented analyses contain more uncertainites and we used reweighting to add the EFT contribution. This makes the new measurements more accurate in the theory uncertainty treatment and provides more conservative results. Another point is to see if we gain more constraining power by not only including measurements from the ATLAS group but also CMS measurements from new physics searches.

We start with an overall comparison between the older results with the two new measurements from 2022, where the CMS ZH process is split up into the two different b tagging categories. In the older measurements the two analyses from 2018 and the two from 2021 are included. The first step is to do an overall comparison

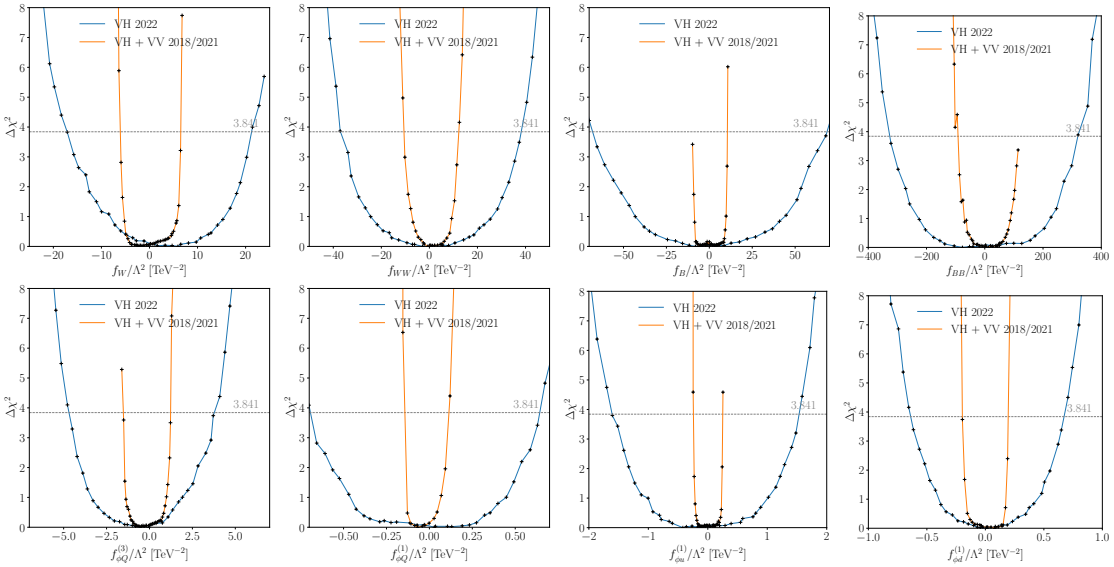

Figure 6.4: Comparing the combination of the 2018 and 2021 measurements (orange) with the 2022 implementation (blue) for all eight coefficients entering in the 2022 VH implementation. The upper row shows the coefficients entering in fermionic operators and the lower row the ones entering in bosonic operators.

involving all coefficients and look if the new measurements are more constraining and in which coefficients we can see an improvement.
Fig. (6.4) displays the corresponding results for the comparison between the previous measurements and the newly implemented ones from this thesis. The upper row shows the Wilson coefficients entering in bosonic operators, while the lower row represents the coefficients entering in fermionic operators. Looking at the results, one can see that the older analyses are more constraining than the newly implemented ones.

So for future comparisons and figures we can use a representative set of three coefficients. These are the ones, that are also involved in the new WH implementation, namely $f_{\phi Q}^{(3)}$, f_W and f_{WW}. With this, all further tests and simulations are much faster than doing the same analyses including all eight coefficients and we still gain valid and comparable results. These results emphasizes the fact that there is no way to know in advance, if newly implemented high kinematic distributions have more constraining power or are an improvement compared to older measurements. It only shows a possible improvement in the end after going through the whole implementation process.

Most constraining measurement

Another interesting question to address is, which one of the previously or old measurements has the strongest constraining power that leads to the results seen in Fig.(6.4). In order to determine this, we can start by comparing the 2018 VH implementations with the ones from 2021 and from 2022. Fig. (6.5) shows the results for the comparison with three coefficents. The blue line represents the VH implementation discussed in this thesis from 2022. The orange line indicates the implementation from the results in 2018 and the green line shows the one from 2021.
For f_W and $f_{\phi Q}^{(3)}$ the VH and VV implementation from 2021 is the most constraining one. Looking at the results for f_{WW}, the VH 2018 implementation is a bit more constraining than the one from 2021 and far more constraining than the one from 2022. The difference between the 2018 and 2021 implementation is rather small for f_{WW}, compared to the improvement in constraining power for the other two coefficients, f_W and $f_{\phi Q}^{(3)}$. Though 2018 has lightly more constraining power on f_{WW}, it is valid to claim the 2021 $VH + VV$ implementation is overall more constraining. So most of the constraining power is coming from the 2021 $VH+VV$ implementation. The next step is to figure out whether the WH or WW process, involved in the 2021 measurement, is more constraining.

The WW implementation consists of only four bins, which makes it harder to start an analysis with three coefficients at a time. Because there are too few bins involved in order to provide stable results for such an anlysis. So for the comparison we have a look at SFitter analyses with only one coefficient involved, to be able to compare them with the WW measurements. This is reasonable for the purpose of comparing the constraining power, since we do not consider the correlation between the various coefficients. The results for the three coefficients, f_W, f_{WW} and $f_{\phi Q}^{(3)}$ are shown in Fig. (6.6).

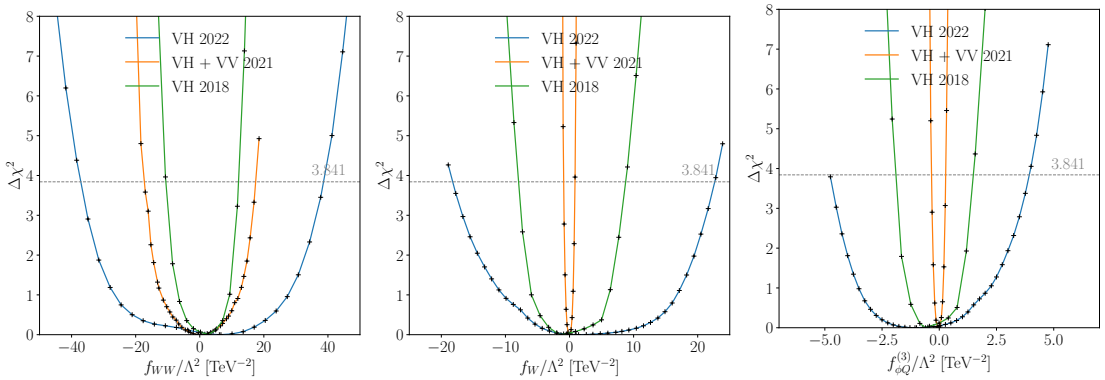

Figure 6.5: Distribution of the 2018 VH implementation (green), the implementation from 2021 (orange) and the one from 2022 (blue). Shown for three coefficients f_{WW} (left), f_W (center) and $f_{\phi Q}^{(3)}$ (right).

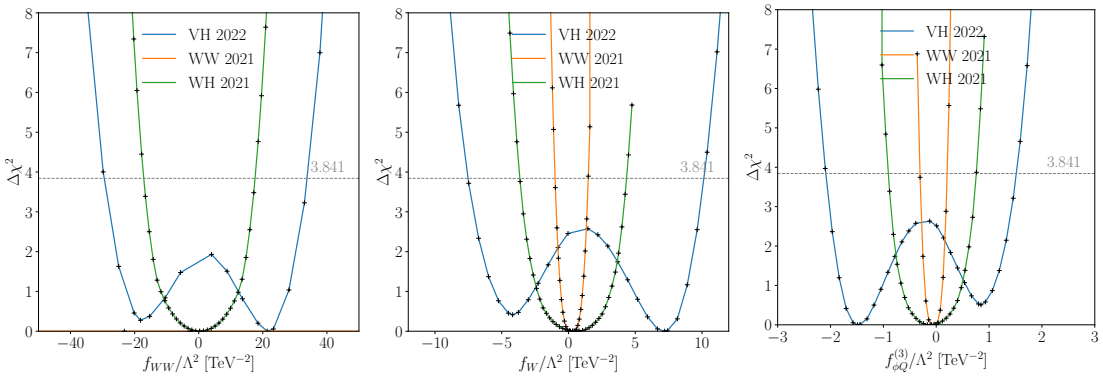

Figure 6.6: Comparing of the two measurements entering in the $VH + VV$ SFitter implementation from 2021. These are a WW and a WH process, both from the ATLAS collaboration. The WW process is indicated by the orange line and the WH one by the green line. As a reference the VH implementation of 2022 is shown with the blue line.

The orange line represents the WW implementation of 2021 and the green line the corresponding WH implementation from 2021, both based on results of the ATLAS collaboration. Next the blue line shows the results from the VH implementation in 2022, described in this thesis. The 2022 VH implementation is only shown as comparison. This is also used to see if the less constraining process from 2021 has still more constraining power than the 2022 implementations.
Most of the constraining power of the 2021 VH implementation is from the WW measurement. Which can be seen for f_W in the central panel and for $f_{\phi Q}^{(3)}$ in the right panel. f_{WW} does not enter the WW prediction and thus only constrained by the WH process. This could explain, why in Fig. (6.5) the implementation of VH in 2018 is more constraining for f_{WW} than the 2021 $VH + VV$ implementation. But both processes have still more constraining power than the VH implementation discussed in this thesis.

So we uncover that implementing high kinematic distributions is a game of luck whether they will be more constraining than the distributions already implemented. In our case it is mostly one process, that dominates the constrains and not the interplay of many measurements. The results are not foreseeable when we start implementing them. So the outcome completely depends on the finer details of the measurements. In order to see first results, we need to reproduce the distribution, reweight it, to add the EFT contribution and then implement everything in SFitter. So one can only see possible improvements in the end, with the first SFitter runs, and not beforehand.

Implementing a whole distribution and only knowing in the end if it was successful and obtains new results is a lot of work, but worth the effort. Because with their large invariant mass range these measurements can give us very powerful constraints

on kinematically enhanced coefficients, as is the case for the most constraining WW distribution of 2021, which is not possible for distributions with lower kinematics. Finally, whether or not the distribution ends up being more constraining than the previous ones, it can still contribute to bettering or understanding of the correlations between coefficients, which is also a very important aspect when we include those measurements in truly global analyses.

7 Summary and Outlook

As stated in the Introduction, there are unsolved problems and open questions regarding physics beyond the SM. Because the scale of new physics might lie far from the reach of current detectors, we should develop indirect ways to explore possible answers. In this thesis, a model-agnostic approach was considered, by parametrizing new physics with an EFT. With the EFT, many new operators and Wilson coefficients are entering the SMEFT framework. These Wilson coefficients can be treated as free parameter and, thus, are constrained by experimental results. In this thesis, we implemented two high kinematic distributions in our SFitter framework and investigated their constraining power on the Wilson coefficients involved.

We studied two experimental results from the LHC. One of them is a WH process studied by the ATLAS collaboration, discussed in chapter 5.1, and the other one is a ZH process from the CMS collaboration, discussed in chapter 5.2. Because both of these high kinematic distributions were intended for resonance searches, there is no SMEFT contribution considered in the experimental data or analysis. Furthermore, the 'default' SMEFT contributions implemented inside SFitter for rate and signal strength measurements in the bulk will not give accurate predictions for the behavior in the high kinematic region. Because of this, we first have to reproduce the distribution and then add the SMEFT contributions on top, by using the reweighting option in MADGRAPH. This reproduction process involves many different components and thus takes a lot of time. It is sometimes made more difficult with missing information in the paper or HEP-data entries. We had to investigate this further to reproduce the results as good as possible. Also we invested some time in the reweighting process with MADGRAPH. It is worth noting that this accurate uncertainty treatment is a strength of SFitter, since it can handle uncertainties of different types and has the ability to correlate them if needed. One of the main goal of this thesis that was successfully accomplished was to keep this uncertainty treatment detailed and conservative for the new high kinematic searches we implemented.
For the WH process, the large theory uncertainties on the signal prediction mean that this analysis does not provide large improvemements on the constraining power on the Wilson coefficients. We have also shown, that considering theory uncertainties as correlated or uncorrelated, has no impact on the constraints. With this in mind we can assume the theory uncertainties as uncorrelated for the WH measurement, without losing constraining power. Because the main constraints are coming from one bin and not from an interplay between them. This conclusion was also reached for high kinematic measurements included in the past, so we feel rather

confident this is generally true. In contrast to the theory uncertainties, a proper underfluctuation treatment improves the constraints on the Wilson coefficients. It is important to take them into account. For a distribution like WH, where more than 50% of the bins have an underfluctuation, the treatment of taking underfluctuations as negative signal prediction into account, has an impact on the results. The newly implemented WH analysis is not more constraining than the old one from 2018, but includes more uncertainties from the experimental results. Also the theory uncertainties are treated more carefully, leading to more precise theory uncertainties in the high kinematic tail region.
The next measurement considered in this thesis is a ZH process from the CMS collaboration. After implementing the ZH measurement in SFitter and looking at the results, we can see that the $2b$ category provides more constraining power than the $\leq 1b$ category. To investigate this further, we had a look on the signal prediction of both categories, and the one from the $2b$ category is way too large compared to the implemented data and background. A reason for this is, that the overall share of the ZH background containing the EFT contribution is larger for the $2b$ category than for the $\leq 1b$ category. Because this is the first implementation of a high kinematic distribution from the CMS collaboration, it cannot be directly compared to older results.

Chapter 6 compares global SMEFT results for different data sets. Starting by comparing the measurements implemented within this thesis, one can see that the WH measurement is more constraining than the ZH measurement. A reason for this could be, that in the WH implementation the most constraining bin has an invariant mass around 2.5 TeV while for the ZH implementation it is around 1.2 TeV. Next the WH and ZH measurements are combined into a global fit and are compared to the results $VH + VV$ analyses from 2018 and 2021. The results from this comparison show that the older analyses are much more constraining than the new measurements. But the VH global analysis from 2022 improved upon previous results by considering the extended theory uncertainty and contributing to correlations between coefficients. Looking further into the implementation from 2021, most of the constraining power there is attributed to a single WW measurement, which then dominates certain parameters. This shows that a single process can dominate certain parameters, not only an interplay of many measurements.

This leads to the following question: is implementing high kinematic distributions worth the effort? On one hand, it is a huge effort, it takes time to implement them into SFitter and, in the beginning, we have no idea whether or not we will gain more constraining power with this process. We are only able to see this with the first SFitter results, after the implementation. On the other hand, if the measurement is more constraining, it can dominate certain Wilson coefficients, especially kinematically enhanced Wilson coefficients. Which means implementing these high kinematic distributions is a bit of a game of luck when looked at through the lens of individual constraints.

However, this is not the only thing we are concerned about with a global SMEFT analysis. This means including high kinematic distributions can still end in two beneficial ways. Either we are not more constraining, but we are able to add a new measurement to our global analysis and thus achieve an improvement in looking at possible correlations between Wilson coefficients, or we gain constraining power on the Wilson coefficients involved. Both outcomes are not a waste of time and help us to better understand the interplay of Wilson coefficients and new physics.
With this in mind, implementing high kinematic distributions is worth the effort, because they allow us to investigate kinematically enhanced coefficients and if we are lucky, they provide us with a huge improvement in constraining power.

Acknowledgments

First and foremost I would like to thank Prof. Tilman Plehn for the great opportunity of working on this project and his support and interest in the work throughout the entire year. I am grateful to Ilaria Brivio, Emma Geoffray and Michel Luchmann for their guidance and support on countless problems throughout this project. In addition I would like to thank all other members of the particle physics phenomenology research group of the ITP for the discussions during lunch and coffee breaks. Thanks also to Lorenz Vogel for his help with the LaTeX version of this thesis. Finally I want to thank Theo for proof reading the thesis, his calmness and support during stressful phases.

Erklärung:

Ich versichere, dass ich diese Arbeit selbstständig verfasst habe und keine anderen als die angegebenen Quellen und Hilfsmittel benutzt habe.

Heidelberg, den (Datum) 26.09.22 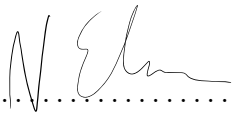

8 References

[1] P. W. Higgs, *Broken Symmetries and the Masses of Gauge Bosons*, Phys. Rev. Lett. **13**, 508 (1964), doi:10.1103/PhysRevLett.13.508.

[2] P. W. Higgs, *Broken symmetries, massless particles and gauge fields*, Phys. Lett. **12**, 132 (1964), doi:10.1016/0031-9163(64)91136-9.

[3] F. Englert and R. Brout, *Broken Symmetry and the Mass of Gauge Vector Mesons*, Phys. Rev. Lett. **13**, 321 (1964), doi:10.1103/PhysRevLett.13.321.

[4] G. Aad *et al.*, *Observation of a new particle in the search for the Standard Model Higgs boson with the ATLAS detector at the LHC*, Phys. Lett. B **716**, 1 (2012), doi:10.1016/j.physletb.2012.08.020, arXiv:1207.7214.

[5] S. Chatrchyan *et al.*, *Observation of a New Boson at a Mass of 125 GeV with the CMS Experiment at the LHC*, Phys. Lett. B **716**, 30 (2012), doi:10.1016/j.physletb.2012.08.021, arXiv:1207.7235.

[6] G. Aad *et al.*, *Combined Measurement of the Higgs Boson Mass in pp Collisions at $\sqrt{s} = 7$ and 8 TeV with the ATLAS and CMS Experiments*, Phys. Rev. Lett. **114**, 191803 (2015), doi:10.1103/PhysRevLett.114.191803, arXiv:1503.07589.

[7] S. Alekhin, A. Djouadi and S. Moch, *The top quark and Higgs boson masses and the stability of the electroweak vacuum*, Phys. Lett. B **716**, 214 (2012), doi:10.1016/j.physletb.2012.08.024, arXiv:1207.0980.

[8] M. Bauer and T. Plehn, *Yet Another Introduction to Dark Matter: The Particle Physics Approach*, vol. 959 of *Lecture Notes in Physics*, Springer, doi:10.1007/978-3-030-16234-4 (2019), arXiv:1705.01987.

[9] J. Schechter and J. W. F. Valle, *Neutrino Masses in SU(2) x U(1) Theories*, Phys. Rev. D **22**, 2227 (1980), doi:10.1103/PhysRevD.22.2227.

[10] D. Bodeker and W. Buchmuller, *Baryogenesis from the weak scale to the grand unification scale*, Rev. Mod. Phys. **93**(3), 035004 (2021), doi:10.1103/RevModPhys.93.035004, arXiv:2009.07294.

[11] S. Weinberg, *Phenomenological Lagrangians*, Physica A **96**(1-2), 327 (1979), doi:10.1016/0378-4371(79)90223-1.

[12] J. Brehmer, *New Ideas for Effective Higgs Measurements*, Ph.D. thesis, U. Heidelberg, doi:10.11588/heidok.00023298 (2017).

[13] A. Biekötter, *Know its limits: A global view on Higgs couplings at the LHC*, Ph.D. thesis, Heidelberg U., doi:10.11588/heidok.00026907 (2019).

[14] T. Corbett, *Effective Lagrangians for Higgs physics*, Ph.D. thesis, Stony Brook U. (2015).

[15] T. Plehn, *Lectures on LHC Physics*, Springer Berlin Heidelberg, doi:10.1007/978-3-642-24040-9 (2012).

[16] D. de Florian *et al.*, *Handbook of LHC Higgs Cross Sections: 4. Deciphering the Nature of the Higgs Sector* **2/2017** (2016), doi:10.23731/CYRM-2017-002, arXiv:1610.07922.

[17] G. Aad *et al.*, *Measurements of the Higgs boson production and decay rates and constraints on its couplings from a combined ATLAS and CMS analysis of the LHC pp collision data at* $\sqrt{s} = 7$ *and 8 TeV*, JHEP **08**, 045 (2016), doi:10.1007/JHEP08(2016)045, arXiv:1606.02266.

[18] S. Dawson, C. Englert and T. Plehn, *Higgs Physics: It ain't over till it's over*, Phys. Rept. **816**, 1 (2019), doi:10.1016/j.physrep.2019.05.001, arXiv:1808.01324.

[19] E. Fermi, *An attempt of a theory of beta radiation. 1.*, Z. Phys. **88**, 161 (1934), doi:10.1007/BF01351864.

[20] D. B. Kaplan, *Five lectures on effective field theory* (2005), arXiv:nucl-th/0510023.

[21] G. Passarino and M. Trott, *The Standard Model Effective Field Theory and Next to Leading Order* (2016), arXiv:1610.08356.

[22] I. Brivio and M. Trott, *The Standard Model as an Effective Field Theory*, Phys. Rept. **793**, 1 (2019), doi:10.1016/j.physrep.2018.11.002, arXiv:1706.08945.

[23] I. Brivio, S. Bruggisser, E. Geoffray, W. Killian, M. Krämer, M. Luchmann, T. Plehn and B. Summ, *From models to SMEFT and back?*, SciPost Phys. **12**(1), 036 (2022), doi:10.21468/SciPostPhys.12.1.036, arXiv:2108.01094.

[24] D. Pappadopulo, A. Thamm, R. Torre and A. Wulzer, *Heavy Vector Triplets: Bridging Theory and Data*, JHEP **09**, 060 (2014), doi:10.1007/JHEP09(2014)060, arXiv:1402.4431.

[25] CMS Collaboration, *Search for a heavy vector resonance decaying to a* Z *boson and a Higgs boson in proton-proton collisions at* $\sqrt{s} = 13$ *TeV*, Eur. Phys. J. C **81**(8), 688 (2021), doi:10.1140/epjc/s10052-021-09348-6, arXiv:2102.08198.

[26] J. Alwall, M. Herquet, F. Maltoni, O. Mattelaer and T. Stelzer, *MadGraph 5: going beyond*, Journal of High Energy Physics **2011**(6) (2011), doi:10.1007/jhep06(2011)128, https://doi.org/10.1007%2Fjhep06%282011%29128.

[27] J. Alwall, R. Frederix, S. Frixione, V. Hirschi, F. Maltoni, O. Mattelaer, H.-S. Shao, T. Stelzer, P. Torrielli and M. Zaro, *The automated computation of tree-level and next-to-leading order differential cross sections, and their matching to parton shower simulations*, Journal of High Energy Physics **2014**(7) (2014), doi:10.1007/jhep07(2014)079, https://doi.org/10.1007%2Fjhep07%282014%29079.

[28] T. Sjöstrand, S. Ask, J. R. Christiansen, R. Corke, N. Desai, P. Ilten, S. Mrenna, S. Prestel, C. O. Rasmussen and P. Z. Skands, *An introduction to PYTHIA 8.2*, Computer Physics Communications **191**, 159 (2015), doi:10.1016/j.cpc.2015.01.024, https://doi.org/10.1016%2Fj.cpc.2015.01.024.

[29] J. de Favereau, , C. Delaere, P. Demin, A. Giammanco, V. Lemaître, A. Mertens and M. Selvaggi, *DELPHES 3: a modular framework for fast simulation of a generic collider experiment*, Journal of High Energy Physics **2014**(2) (2014), doi:10.1007/jhep02(2014)057, https://doi.org/10.1007%2Fjhep02%282014%29057.

[30] R. Lafaye, T. Plehn, M. Rauch and D. Zerwas, *Measuring supersymmetry*, The European Physical Journal C **54**(4), 617 (2008), doi:10.1140/epjc/s10052-008-0548-z, https://doi.org/10.1140%2Fepjc%2Fs10052-008-0548-z.

[31] P. de Aquino, W. Link, F. Maltoni, O. Mattelaer and T. Stelzer, *ALOHA: Automatic libraries of helicity amplitudes for feynman diagram computations*, Computer Physics Communications **183**(10), 2254 (2012), doi:10.1016/j.cpc.2012.05.004, https://doi.org/10.1016%2Fj.cpc.2012.05.004.

[32] L. Lista, *Statistical Methods for Data Analysis in Particle Physics*, vol. 909, Springer, ISBN 978-3-319-20175-7, 978-3-319-20176-4, doi:10.1007/978-3-319-20176-4 (2016).

[33] B. Andersson, G. Gustafson, G. Ingelman and T. Sjostrand, *Parton Fragmentation and String Dynamics*, Phys. Rept. **97**, 31 (1983), doi:10.1016/0370-1573(83)90080-7.

[34] M. Cacciari, G. P. Salam and G. Soyez, *FastJet User Manual*, Eur. Phys. J. C **72**, 1896 (2012), doi:10.1140/epjc/s10052-012-1896-2, arXiv:1111.6097.

[35] S. Catani, Y. L. Dokshitzer, M. H. Seymour and B. R. Webber, *Longitudinally invariant K_t clustering algorithms for hadron hadron collisions*, Nucl. Phys. B **406**, 187 (1993), doi:10.1016/0550-3213(93)90166-M.

[36] *A Cambridge-Aachen (C-A) based Jet Algorithm for boosted top-jet tagging* (2009).

[37] M. Cacciari, G. P. Salam and G. Soyez, *The anti-k_t jet clustering algorithm*, JHEP **04**, 063 (2008), doi:10.1088/1126-6708/2008/04/063, arXiv:0802.1189.

[38] A. Gelman, J. B. Carlin, H. S. Stern and D. B. Rubin, *Bayesian Data Analysis*, Chapman and Hall/CRC, 2nd ed. edn. (2004).

[39] I. Brivio, S. Bruggisser, N. Elmer, E. Geoffray, M. Luchmann and T. Plehn, *To Profile or To Marginalize – A SMEFT Case Study* (2022), arXiv:2208.08454.

[40] ATLAS Collaboration, *Measurements of gluon fusion and vector-boson-fusion production of the Higgs boson in $H \to WW^* \to e\nu\mu\nu$ decays using pp collisions at $\sqrt{s} = 13$ TeV with the ATLAS detector* (2021), `https://cds.cern.ch/record/2759651`.

[41] A. Biekoetter, T. Corbett and T. Plehn, *The Gauge-Higgs Legacy of the LHC Run II*, SciPost Phys. **6**(6), 064 (2019), doi:10.21468/SciPostPhys.6.6.064, arXiv:1812.07587.

[42] M. Aaboud *et al.*, *Search for heavy resonances decaying into a W or Z boson and a Higgs boson in final states with leptons and b-jets in 36 fb^{-1} of $\sqrt{s} = 13$ TeV pp collisions with the ATLAS detector*, JHEP **03**, 174 (2018), doi:10.1007/JHEP03(2018)174, [Erratum: JHEP 11, 051 (2018)], arXiv:1712.06518.

[43] G. Aad *et al.*, *Search for resonances decaying into a weak vector boson and a Higgs boson in the fully hadronic final state produced in proton−proton collisions at $\sqrt{s} = 13$ TeV with the ATLAS detector*, Phys. Rev. D **102**(11), 112008 (2020), doi:10.1103/PhysRevD.102.112008, arXiv:2007.05293.

[44] G. Aad *et al.*, *Search for heavy diboson resonances in semileptonic final states in pp collisions at $\sqrt{s} = 13$ TeV with the ATLAS detector*, Eur. Phys. J. C **80**(12), 1165 (2020), doi:10.1140/epjc/s10052-020-08554-y, arXiv:2004.14636.

[45] M. Aaboud *et al.*, *Evidence for the $H \to b\bar{b}$ decay with the ATLAS detector*, JHEP **12**, 024 (2017), doi:10.1007/JHEP12(2017)024, arXiv:1708.03299.